Source-Parameter Estimation after Attenuation Correction through the Use of Q Tomography

Pasquale De Gori[*1] , Francesco Pio Lucente[1] , and Claudio Chiarabba[1]

ABSTRACT

The measurement of earthquake source parameters is affected by large uncertainties, and different approaches lead to large variability in results. One crucial aspect is the trade-off between attenuation (Q) and corner frequency (f_c) in spectral fitting: The source corner frequency, inversely proportional to the fault size, can be severely masked by attenuation and site effects. In this article, we describe a method to solve the trade-off based on the fit of displacement spectra to find the source characteristics (corner frequency, f_c, and the signal moment, Ω_0) and the single-station attenuation operator ($t*$), in addition to the site response. We follow a parametric approach based on the use of 3D Q seismic tomography and a bootstrap-based method for selecting the best spectra fit. The correction of attenuation with synthetic values derived by 3D attenuation tomography efficiently deals with the trade-off between source and path terms, leading to small uncertainties in the determination of source unknowns (f_c and signal moment, Ω_0), thus yielding constrained estimates of source parameters for low- to medium-magnitude earthquakes. We show an application to the Emilia 2012 seismic sequence, for which we computed the source parameters for 1240 aftershocks (from an initial dataset of 1748) with local magnitude ranging from 2.0 to 4.7 using the spectral fit from P and S waves. About 80% of stress-drop estimations are characterized by relatively low uncertainties (within 20% of the estimated values), with maximum values of about 40% for the remaining 20%. The attenuation correction is effective to determine source parameters for small-magnitude earthquakes; hence, we obtain reliable estimates of source parameters for the entire aftershock sequence. This approach gives the opportunity to infer the mechanical state of a complete fault system by taking advantage of the larger number of low-magnitude events (with respect to the largest ones) that always follow a major earthquake.

KEY POINTS

- We apply Q_P and Q_S tomography to correct the component of spectral decay related to attenuation effects.
- The proposed approach leads to stable source-parameter estimation even for small-magnitude earthquakes.
- This study may stimulate a thorough analysis of both past and future aftershock sequences source parameters.

Supplemental Material

INTRODUCTION

The determination of seismic source parameters (seismic moment, source dimension, stress drop) plays an important role in studying earthquake physics, for example, to define fault interaction or to predict the ground shaking (i.e., Boore, 1983). Following the basic theoretical relationship that relates static stress drop to seismic moment and source dimension (Eshelby, 1957; Brune, 1970; Kanamori and Anderson, 1975), their computation may appear a trivial task. However, reliable estimation of source parameters remains problematic, leading to controversial assumptions about the source scaling of earthquakes. It is commonly accepted that, for large earthquakes, seismic moment scales with fault dimension and stress drop remain almost constant (Aki, 1967; Stein and Wysession, 2009). Conversely, for small- to moderate-size events, different views have been argued. Some authors suggested that stress drop increases with the size of earthquakes (e.g., Mayeda and Walter, 1996; Mayeda *et al.*, 2007), whereas others conclude that self-similarity holds even for small-magnitude events (e.g., Abercrombie, 1995; Imanishi and Ellsworth, 2006). Therefore, a large variability persists in source-parameter studies that arise from the determination of source dimensions

and the correction of the observed signal for attenuation and site effect.

In fact, in the far-field approximation, the observed seismograms or, equivalently, the shape of the observed spectral amplitudes, are the results of the interaction of three contributes: (1) the source, (2) the along-path attenuation, and (3) the site response (i.e., Stein and Wysession, 2009).

To perform source analysis, the observations (seismograms or spectra) must be "cleaned" of terms (2) and (3), and, under the assumption that the shape of the fault is rectangular or circular (Kanamori and Anderson, 1975), the event seismic moment, the source dimension, and the static stress drop (called static source parameters) are usually computed.

One big problem in obtaining reliable measurements deals with the correction for path attenuation and site response that are in trade-off with source terms (Boatwright et al., 1991; Ko et al., 2012; Zollo et al., 2014; Abercrombie, 2021). Different approaches are adopted to address this issue. Abercrombie (2021) made a wide and complete review of all the methods currently used to face this problem and to estimate source parameters, describing the assumptions and the limitations of each method.

Here, we synthesize some crucial aspects for a comparison with the methodology we adopted.

One strategy in use to correct path, site, and the frequency dependence of attenuation relies on the empirical Green function (EGF) from seismic events with similar locations (e.g., Hough, 1997; Hough, 2001; Ide et al., 2003; Imanishi and Ellsworth, 2006). Given a couple of events, close in space but with a considerable difference in magnitudes (see, for details, Abercrombie, 2021), the smallest event acts as EGF for the more energetic one. This approach requires that earthquakes are colocated and significantly different in size (Abercrombie, 2015, 2021), with impact on the applicability for a limited dataset of events. Further applications of EGF methods are based on the spectral stacking of large number of events occurred in clusters or at larger scale to isolate the source terms (e.g., Prieto et al., 2004; Shearer et al., 2006; Allmann and Shearer, 2007; Trugman and Shearer, 2017). In general, the removal of path effects with spectral ratio requires some assumption on attenuation homogeneity within the rock volume.

Recently, Yoshimitsu et al. (2019) (hereinafter YEA) proposed a method based on the coda-wave spectral ratios between a large-magnitude event and a small event acting as EGF. The stacks of all the spectral ratios are used to extract the two corner frequencies of the couple of events and their moment ratio. This method gives robust estimation of stress drop and reliable uncertainty measurements.

An alternative approach is to filter the path and site terms by a spectral inversion scheme, using either a nonparametric or parametric approach. The main difference is the correction used for the attenuation term. In a nonparametric scheme,

the attenuation term is computed by a model that, for each analyzed frequency, consists in a smooth function of distance obtained by inverting the spectral observations (e.g., Bindi et al., 2004; Oth et al., 2008; Oth et al., 2011, Picozzi et al., 2017). In the parametric approach, the attenuation and the source model are used as a priori information (e.g., Edwards et al., 2008). The attenuation term is computed in a 3D tomographic model that constrains the geometry and the spatial variability of the Q structure (Rietbrock, 2001, Edwards et al., 2008; Koulakov et al., 2010) leading to more realistic attenuation corrections with respect to a uniform Q model (Lees and Lindley, 1994; Tsumura et al., 2000; Rietbrock, 2001).

In this article, we developed a methodology that follows this latter parametric approach, in which, in a multistep calculation scheme, the output of each step is used as input for the next step.

The first part of our procedure relies on the fit of P- and S-wave observed spectra, as described in Stachnik et al. (2004), in which all the spectra of one event are simultaneously used to find the source characteristics (f_c and seismic moment) and single-station attenuation decays. In the second part, we compute a 3D attenuation structure for P and S waves using a 3D velocity model and 3D earthquake locations as described in Rietbrock (2001). In the last part, the attenuation factors computed in the Q_P and Q_S tomographic model are used to correct the spectra, and to find the source parameters using P and S waves separately.

Furthermore, we compare our S-wave f_c estimations with those derived by applying the method of YEA, in which coda-wave spectral ratios are used. We apply both our method and the YEA method to the aftershocks sequence of the 2012 Emilia earthquakes (Scognamiglio et al., 2012) using the seismograms recorded at local distances by the permanent and temporary stations deployed in the epicentral area (Govoni et al., 2014).

GENERAL FORMULAE FROM THEORY

The far-field velocity spectrum, $V_{ij}(f)$, observed at a station (ith) from the earthquake jth is the result of different physical processes occurring at the source along the ray path and at the recording site. These different contributions in the frequency domain are expressed by multiplicative terms (e.g., Scherbaum, 1990):

$$V_{ij}(f) = 2\pi f S_i(f) A_{ij}(f) R_j(f) I_j(f), \tag{1}$$

in which S_i is the source spectrum of the ith event; A_{ij} is the attenuation term; R_j is the site response dependent on the shallow geology structure beneath the recording site; and I_j is the instrument transfer function in terms of poles and zero used to correct all seismograms for the instrumental response. The term $2\pi f$ is a factor needed to express the velocity spectral amplitudes.

The displacement source spectrum in the far-field approximation is

$$S_i(f) = \Omega_0 \frac{f_c^{\gamma}}{f_c^{\gamma} + f^{\gamma}}, \tag{2}$$

in which Ω_0 represents the low-frequency level depending on the seismic moment (Aki, 1967), and f_c is the source corner frequency, which is inversely proportional to the source dimension; gamma quantifies the source spectral decay at frequencies higher than f_c. In this study, we set the spectral fall-off equal to 2 (see the following paragraph).

The attenuation term quantifying the attenuation along the ijth ray path is

$$A_{ij}(f) = \exp[-\pi t^* f^{(1-\alpha)}], \tag{3}$$

in which t^* is the ratio between travel times and quality factor Q, and depends from the velocity and the attenuation structure of the medium traveled by seismic energy; α quantifies the dependency of quality factor Q from frequency and assumes values from 0 to 1.

In agreement with the previous studies (Adams and Abercrombie, 1998; Rietbrock, 2001), for lower magnitude events (higher frequencies), we found a weak to null dependence of Q from the frequency, whereas for the class of the largest magnitudes (M_L 4.0–5.0), a dependency of Q from the frequency is observed (see Fig. S1, available in the supplemental material to this article, and its description, for further details).

In this study, we chose to set $\alpha = 0.0$, that is, consider Q frequency independent, because the vast majority of the analyzed events belongs to the lower magnitude classes 2–3 and 3–4 (see Table 1): We are therefore confident that setting $\alpha = 0$ is a licit assumption as already stated in the previous studies based on spectral modeling and attenuation tomography (e.g., Boatwright et al., 1991; Rietbrock, 2001; Edwards et al., 2008). Furthermore, the use of frequency-dependent Q (i.e., varying the α values) would imply several attenuation models (e.g., Koulakov et al., 2011), resulting into a complexity that is beyond the scope of this work.

Inserting in equation (1) the terms expressed by equations (2) and (3), the observed spectrum, corrected for $I_j(f)$, may be expressed as

$$\log_{10}\left[\frac{V_{ij}(f)}{2\pi f}\right] = \log_{10}[\Omega_0] + \log_{10}\left[\frac{f_c^{\gamma}}{f_c^{\gamma} + f^{\gamma}}\right]$$
$$- 0.434\pi\, t^*[f^{(1-\alpha)}]. \tag{4}$$

We refer to this equation to describe the modeling methodology. Using all the spectral observations for a seismic event, we find a common source corner frequency f_c and, for each single station, the attenuation operator (t^*) and low-frequency level (Ω_0). This approach has been previously introduced by Stachnik et al. (2004), and applied to P- and S-wave spectra of subduction seismic events.

TABLE 1
Number of Events Selected in the Three Steps of the Workflow (In Parentheses Number of Events With Source Parameters Estimation)

Magnitude Ranges	Step		
	Step 01	Step 02	Step 03
2–3 P waves	234 (205)	415 (393)	1074 (1061)
3–4 P waves	95 (95)	138 (138)	143 (143)
4–5 P waves	5 (5)	6 (6)	3 (3)
2–3 S waves	665 (663)	785 (785)	1029 (1029)
3–4 S waves	136 (136)	146 (146)	134 (134)
4–5 S waves	8 (8)	9 (9)	9 (8)

The estimated values of these unknowns (f_c, t^*, Ω_0) for P- and S-wave spectra are subsequently used to compute the source parameters assuming the circular crack model of Brune (1970). We compute the seismic moment (M_0), the fault radius (r), and static stress drop ($\Delta\sigma$) by the following relations:

$$M_0 = \frac{4\pi\rho V_S^3 D\Omega_0}{FR_{\vartheta\phi}}, \tag{5}$$

$$r = \frac{Kp,s(V_S)}{f_{cPS}}, \tag{6}$$

$$\Delta\sigma = \frac{7}{16}\frac{M_0}{r^3}. \tag{7}$$

Assuming that, in these equations, the same letters have the same physical meaning, as in equation (5), Ω_0 is the low-frequency level of the displacement spectrum of the analyzed phases, D is the epicentral distance, and ρ and V_S are the density and S-wave velocity of the medium, respectively. R is the average radiation pattern coefficient equal to 0.52 and 0.62 for P and S waves, respectively (Boore and Boatwright, 1984), and F is the free-surface amplification set to 2. In equation (6), Kp,s is a constant that depends on the adopted circular model, and according to the Madariaga model, its value is 0.32 and 0.21 for P and S waves, respectively (Madariaga, 1976).

To compute the error on stress-drop determinations, we account for the errors related to all the variables that enter in equation (7). Thus, the error on the seismic moment (or low-frequency level as in equation 5) and seismic radius (function of f_c) are the input for the estimation of stress-drop uncertainty that, following Fletcher et al. (1984), may be expressed by

$$\left(\frac{\sigma_{\text{sd}}}{\Delta\sigma}\right)^2 = \left(\frac{\sigma_M}{M_0}\right)^2 + 9\left(\frac{\sigma_r}{r}\right)^2, \tag{8}$$

in which σ_{sd}, σ_M, and σ_r are the uncertainties on stress drop, seismic moment, and seismic radius, respectively, whereas $\Delta\sigma$, M_0, and r are the corresponding absolute estimates.

DATASET

The Emilia 2012 seismic sequence developed along the compressional system of the Apennines on the central portion of the Ferrara front (Fig. 1).

The sequence was characterized by two main thrust earthquakes (M_L 5.9, 20 May 2012, 02:03 UTC; M_L 5.8, 29 May 2012, 07:00 UTC) that activated an almost 50 km long fault system elongated in west–east direction. Most of the seismicity was located beneath the Po plain alluvial sediments at depths ranging from 5 to 10 km (Chiarabba et al., 2014, Pezzo et al., 2018). After the occurrence of the first mainshock, a dense array of temporary stations was deployed in the epicentral region to follow the spatial and temporal evolution of the seismic sequence. For this study, we use a total of 1748 aftershocks as initial dataset, with 22,544 P and 15,179 S phases handily analyzed for accurate estimation of the P and S phases onset (Govoni et al., 2014), and used for V_P and V_P/V_S tomography and earthquake locations (Chiarabba et al., 2014; Pezzo et al., 2018; Fig. 1).

The waveforms analyzed in this work are available through the European Integrated Data Archive (EIDA) web services (see Data and Resources; Strollo et al., 2021). We extract P- and S-wave amplitude spectra of seismograms recorded at local distances by velocity seismometers with natural periods of 40 s (HH channels, following the convention of EIDA, for Italian archive; see Strollo et al., 2021) and 5 s (EH channels), for permanent and temporary stations, respectively (see Data and Resources). All the waveforms are sampled at 100 Hz.

The records are corrected for instrumental response quantified by poles and zeros of transfer function using the standard Seismic Analysis Code routines (Goldstein and Snoke, 2005; Helffrich et al., 2013). The magnitude (M_L) interval of the events ranges from 1.4 to 5.6.

Because the bandwidth limitation imposed by the waveforms sample rate (100 Hz) limits the estimation of the corner frequency for frequencies above the antialias filter corner frequency (40 Hz), we restrict our analysis to earthquakes with magnitude $M_L \geq 2$ (1306 events). Most of the used aftershocks (1141) have magnitudes $2 \leq M_L < 3$, whereas the remnant dataset consists of 151 events in the range $3 \leq M_L < 4$, and 14 with $M_L \geq 4$.

To complete our analysis, we also compute the source parameters of the most energetic events of the sequence consisting of two mainshocks (M_L 5.9, 20 May 2012, 02:03 UTC; and M_L 5.8, 29 May 2012, 07:00 UTC) and three additional **M** 5+ events (M_L 5.1, 20 May 2012, 03:02 UTC; M_L 5.2, 20 May 2012, 13:18 UTC; and M_L 5.0, 3 June 2012, 19:20 UTC; see Fig. 1). These earthquakes are not included in the bulk of aftershocks but are processed separately using only S-wave spectra for the following motivations: The spectral analysis of an **M** 5+ event requires time windows above 10 s due to the low-frequency content of the seismic signal; for P-wave spectra analysis, such time windows require an S–P time of at least 10 s that is compatible with epicentral distances greater than 45–50 km, that is, outside the tomographic model (see Pezzo et al., 2018)

that we use to locate the aftershocks and to correct the seismic spectra for attenuation; to apply a similar tomographic correction for stations farther than 50 km, a 3D tomographic model at regional scale is required, and although different regional velocity models have been determined for Italy (Di Stefano et al., 2009; Scafidi et al., 2009), no attenuation models have been published so far.

For such events, we use stations deployed in the Alps, north of the epicentral region, and in the northern Apennines, on the south, at distances from 50 to 250 km. For the two mainshocks, we use stations at epicentral distance up to 600 km. For these events, the attenuation correction of the observed spectra is performed using the Q estimated from the spectral high-frequency decay, as is done for all the analyzed events at the step 01 of the multistep procedure described in the next section.

To compute P- and S-wave spectra, we isolated a time window that is a function of the magnitude on the vertical (P wave) and transverse (S wave) components of seismograms (Abercrombie, 1995). For the smallest events ($2 \leq M_L < 3$), we use time windows of 1.28 s that are increased to 2.56 and 5.12 s for events in the magnitude interval 3–4 and 4–5, respectively (see Table 2). For the largest events ($M_L > 5$), we use a time window of 10.24 s. For P-wave time windows, to prevent contamination by S-wave arrivals, we select only those seismograms in which the differential times between S and P phases is greater than the selected P time window.

After tapering the time window to reduce the effects of limited record lengths, we compute the spectral content using the FFT. A Hanning window is then used to smooth the resulting spectrum. To evaluate the noise level, we applied the same procedure on a time window of the same length preceding the P-wave signal. We use the same noise window for the P and S signals.

The spectral band usable for the analysis begins from the smallest frequency resolvable by the used time length and extends to the antialiasing digitizer filter (40 Hz). For a spectrum to be usable, we search for a continuous long band in which the signal-to-noise ratio (SNR) is greater than 1.5. This band is chosen depending on the magnitude interval of the events and on the type of computation that we are performing (Table 2). The threshold of 1.5 for the SNR has been chosen, because we are interested in determining the source parameters of smaller earthquakes, and has been applied only to waveforms that have been previously accurately picked (see Govoni et al., 2014). This still permits to retain good-quality spectral amplitudes for robust identification of spectral parameters (examples for a lower magnitude event, $M_L \approx 2$, are pictured in Fig. S2).

Spectral fit for f_c, Ω_0, and t^* determination

P and S spectra are processed separately using the same procedure. For a generic seismic event, we use simultaneously all the P- or S-wave spectra that meet the SNR selection criteria, and we apply a grid search at 0.1 Hz steps, over the complete frequency range, within the antialiasing digitizer filter (40 Hz),
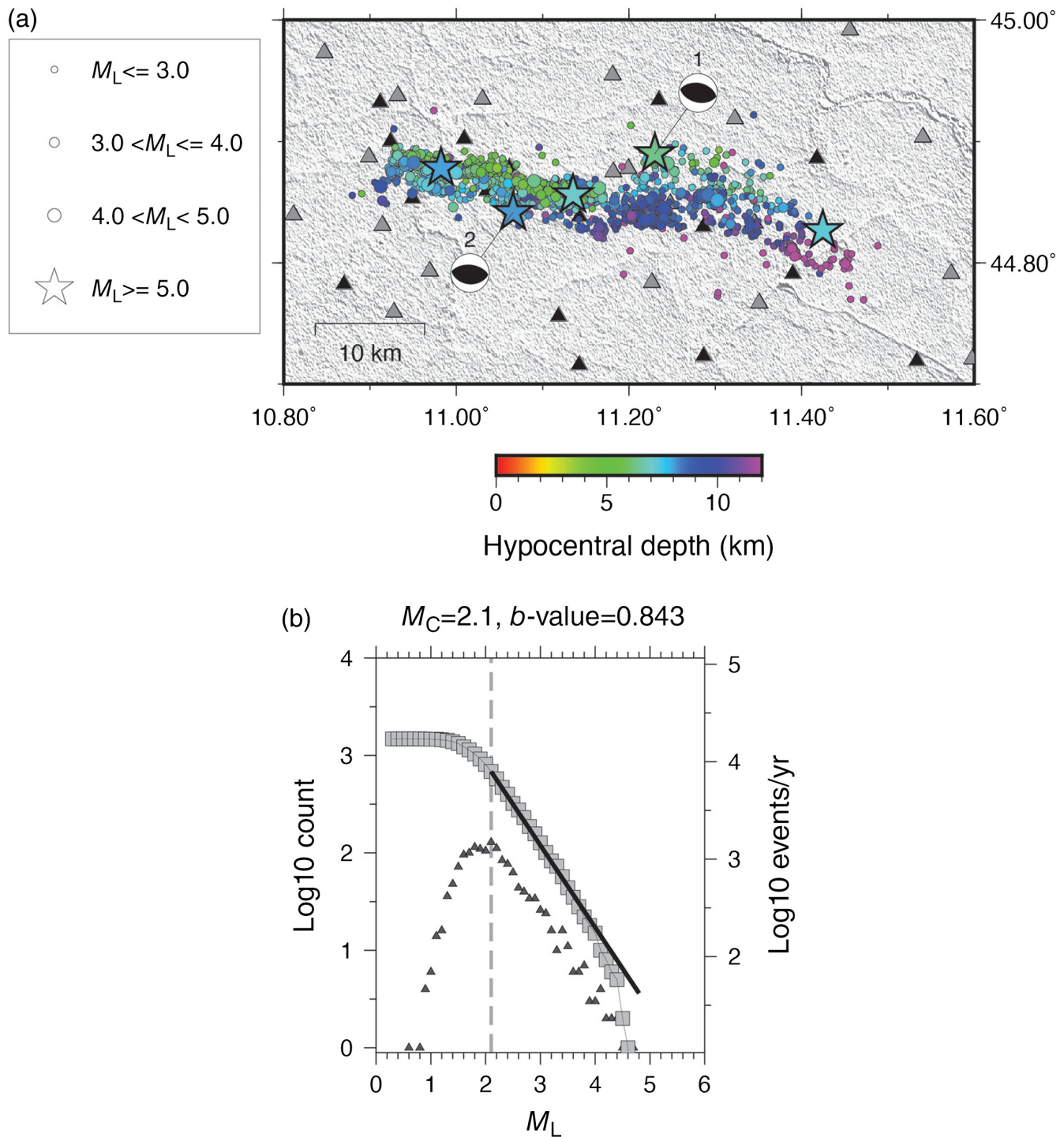
Figure 1. (a) Spatial distribution of the aftershocks used in this work. Hypocentral depths are differentiated by the color code, whereas the circle size is proportional to the event magnitude according to the scheme on the left of the map. The largest (**M** > = 5.0) events are drawn by stars. The two mainshocks are also indicated by the time domain moment tensor (TDMT) focal-plane solutions (Scognamiglio *et al.*, 2012). Black and gray triangles are, respectively, the permanent and temporary seismic stations operating in the area during the 2012 Emilia seismic sequence. (b) Frequency–magnitude distribution of the used aftershocks. The cumulative and noncumulative numbers of earthquakes are shown by light gray squares and dark-gray triangles, respectively. The gray, dashed line indicates the completeness magnitude value (2.1), whereas the black line represents the maximum-likelihood fit to the data for magnitudes above the magnitude of completeness at 95% level (Wiemer and Wyss, 2000); the slope of the black line is the *b*-value of the Gutenberg–Richter law. The color version of this figure is available only in the electronic edition.

TABLE 2
Frequency Bands, Time Windows and Magnitude Ranges in the Three Steps of the Workflow

| Magnitude Ranges and Time Windows | Step | | |
	Step 01 (Site Correction)	Step 02 (t* for Tomo Q)	Step 03 (Source Parameter)
2–3 (1.28 s)	1–40 Hz (whole band)	1–40 Hz (band length: 30 Hz)	1–40 Hz (band length: 30 Hz)
3–4 (2.56 s)	0.2–40 Hz (whole band)	0.2–40 Hz (band length: 30 Hz)	0.2–40 Hz (band length: 30 Hz)
4–5 (5.12 s)	0.1–40 Hz (whole band)	0.1–40 Hz (band length: 30 Hz)	0.1–40 Hz (band length: 30 Hz)
5–5.5 (10.24 s)	0.05–40 Hz (band length: 20 Hz)		
5.8–6.0 (Mainshocks, 40.96 s)	0.03–30 Hz (band length: 20 Hz)		

Tomo Q, Q tomography.

computing the event f_c, common to all the stations, and single stations Ω_0 and t^* (see Table 2, for the chosen frequency ranges).

For each frequency assumed as trial f_c, we correct the observed spectrum subtracting the second addend of the right side of equation (4) from the left side of equation (4). Thus, the corrected spectrum $C_{ij}(f)$ of the station jth is

$$C_{ij}(f) = \log_{10}\left[\frac{V_{ij}(f)}{2\pi f}\right] - \log_{10}\left[\frac{f_c^\gamma}{f_c^\gamma + f^\gamma}\right], \qquad (9)$$

and equation (4) reduces to

$$C_{ij}(f) = \log_{10}[\Omega_0] - 0.434\pi\, t^*[f^{(1-\alpha)}]. \qquad (10)$$

This is the equation of a straight line in the form $C_{ij}(f)$ versus $f^{(1-\alpha)}$, in which the slope is $-0.434 \cdot \pi \cdot t^*$, and the intercept is $\log_{10}[\Omega_0]$.

We perform for each station j a linear regression of $C_{ij}(f)$ as function of $f^{(1-\alpha)}$ to find the unknown parameters of the straight line (Stachnik *et al.*, 2004). From the slope, we estimate the t^* along the path ijth, whereas the intercept is used to find the low-frequency plateau Ω_0. The goodness of the trial f_c is quantified by computing a cost function that accounts for the difference between observed and theoretical spectral amplitudes for all the spectra of the event. Following Edwards *et al.* (2008) and de Lorenzo *et al.* (2010), we use as cost function the root mean square (rms) of amplitudes that in L2 norm is defined as
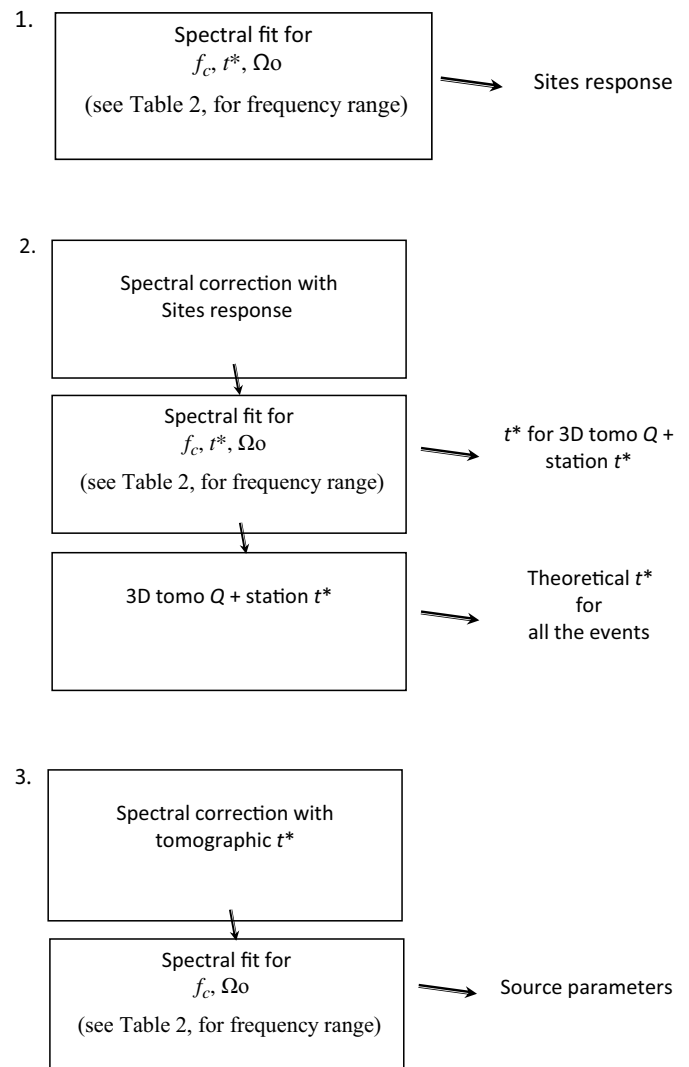
$$\mathrm{rms} = \sqrt{\frac{1}{N}\sum_{j=1}^{N}(V_{ij}^{\mathrm{obs}} - V_{ij}^{\mathrm{th}})^2}, \qquad (11)$$

in which V_{ij}^{obs} and V_{ij}^{th} are the observed and theoretical amplitudes estimated by the computed parameters (the assumed f_c, and single station Ω_0 and t^*), and N is the number of the discrete frequencies over which the summation is computed. All the rms values computed for each trial f_c define the misfit function (MF). The event f_c is the frequency for which we observe the minimum of MF.

Method: Multistep procedure

Our procedure consists in resolving the f_c–t^* trade-off with a progressive refinement of parameters from a first fit of velocity

spectra for extracting site response at each station from residuals amplitude of spectra fit (step 01). Then, with the estimated site response, we refine the spectral fit for t^* and compute a 3D attenuation tomography (step 02). Finally, with the theoretical t^* computed within the 3D Q model, we refine the computation of f_c and source parameters (step 03). The entire procedure is summarized in the following scheme:

1.

Spectral fit for
f_c, t^*, Ωo

(see Table 2, for frequency range) → Sites response

2.

Spectral correction with
Sites response

↓

Spectral fit for
f_c, t^*, Ωo

(see Table 2, for frequency range) → t^* for 3D tomo Q + station t^*

↓

3D tomo Q + station t^* → Theoretical t^* for all the events

3.

Spectral correction with
tomographic t^*

↓

Spectral fit for
f_c, Ωo

(see Table 2, for frequency range) → Source parameters

In all the described steps, we fit the spectra using the grid-search method illustrated earlier, whereas the frequency band that we used depends on the type of computation, as summarized in Table 2.

Examples of the fitting procedure in the three different steps are shown for the P and S waves, respectively, in Figures S2–S4.

The most important aspect of studies focused on the determination of source parameters is related to the estimation of f_c and of its errors. We discuss this point in a dedicated section (see the following).

We now describe in more detail each step of the adopted procedure.

Method step 01: Computation of site response

We select all the P- and S-wave spectra, in which the SNR is above the threshold in the complete resolvable frequency band according to Table 2. Then, we compute the event f_c and the single station Ω_0 and t^*, with a grid search over the complete frequency band resolvable by the used time window (Table 2).

Once we find the best fit model for each event, we compute the site amplification $R_j(f)$ following the method of Tsumura *et al.* (1996), Edwards *et al.* (2008), and Edwards and Rietbrock (2009). The site response spectrum is expressed by the average of residuals obtained at discrete frequencies considering all the spectra recorded by each station. It is defined by

$$\log_{10}[R_j(f)] = \frac{1}{N}\sum_{i=1}^{N}\log_{10}\left[\frac{V_{ij}^{\mathrm{obs}}}{V_{ij}^{\mathrm{th}}}\right], \qquad (12)$$

in which N is the number of events recorded by the station jth.

The average over a large number of spectra with different azimuthal paths can be considered a proxy of the near site structure beneath each seismic station.

Method step 02: Computation of t^* and attenuation tomography

The second step consists in the estimate of t^* and the computation of the 3D Q model. In this step, we reselect all the spectra searching for a continuous band, in which the SNR is greater than the threshold within the analyzed frequency band (Table 2). This choice enables to increase the number of spectra usable for tomography without decreasing the quality of the dataset. We use the site correction $R_j(f)$, as computed in step 01, as a priori information in equation (1) to correct the observed spectrum for shallow effects. Then, we applied the same grid search described previously for computing f_c and t^* values.

The goodness of the final fit is quantified by the rms that is also used to assign data weights for the Q inversion (weights of 0, 1, 2, and 3 for rms less than 0.1, 0.2, 0.3, and 0.4, respectively, following Eberhart-Phillips and Chadwick, 2002). t^* values are discarded if rms is equal or greater than 0.4 and in the few cases, in which the t^* lead to unrealistic Q_P and Q_S values ($Q > 5000$).

We select a total of 5021 t^* from 526 events and 8079 t^* from 940 events for Q_P and Q_S inversion, respectively. The inversion of t^* for the 3D Q_P and Q_S structure is based on the following relationship:

$$t^* = \int_{\mathrm{raypath}} \frac{dr}{V_{(r)}Q_{(r)}} + t_{\mathrm{site}}^*, \qquad (13)$$

in which $V(r)$ and $Q(r)$ are the velocity and the quality factor along the segments of ray with length dr. The term t^* site accounts for the shallow attenuation beneath the recording site (that may have strong influence on the observed spectrum and differs from the site response $R_j(f)$). Because rays are traced in a known 3D velocity model, t^* only depends on the Q structure. Hypocenters located within the 3D velocity model are, at this point, kept fixed and equation (13) is solved, similarly to travel-time tomography, to find the Q structure (see Rietbrock, 2001). The tomographic model is represented by a grid of nodes and the inversion is carried out by an iterative damped least-squares approach, in which Q values are updated at each iteration, whereas velocity values remain fixed to their starting heterogeneous values (Rietbrock, 2001).

Method step-03: Spectral correction with Q tomography (tomo Q) and computation of source parameters

After the determination of the Q models, we compute the synthetic t^* by tracing all the seismic rays of our dataset within the 3D velocity and Q model. It is noteworthy that the number of synthetic t^* is greater than t^* inverted for tomography, because the real data underwent a selection process that diminishes its amount. Hence, at this point of the workflow, all the observed spectra have their correspondent synthetic t^*, although some of them did not contribute to defining 3D Q structure.

In this final step, for each event, we fit the spectra fixing the attenuation term to that obtained in the 3D Q (Q_P or Q_S) structure. The spectral modeling is carried out using the same selection criteria adopted in step 02 (Table 2). We perform a grid search to find the optimal f_c for P- and S-wave spectra. For each trial f_c, we apply equation (10) keeping t^* fixed to the tomographic value, and we find the unique unknown represented by the low-frequency level Ω_0 at each station. This approach strongly increases the precision of f_c determination and allows to retrieve many spectra previously discarded for bad fitting quality (see the following).

Step 01: Results (site response)

In Figure 2a, we show some representative examples of site responses computed by equation (12) for P- and S-wave spectral fit. For a generic seismic station, all the residuals between the observed and theoretical amplitude are averaged at each frequency, thus reducing the effect related to the source and outlining the contribution of the shallow structure beneath the
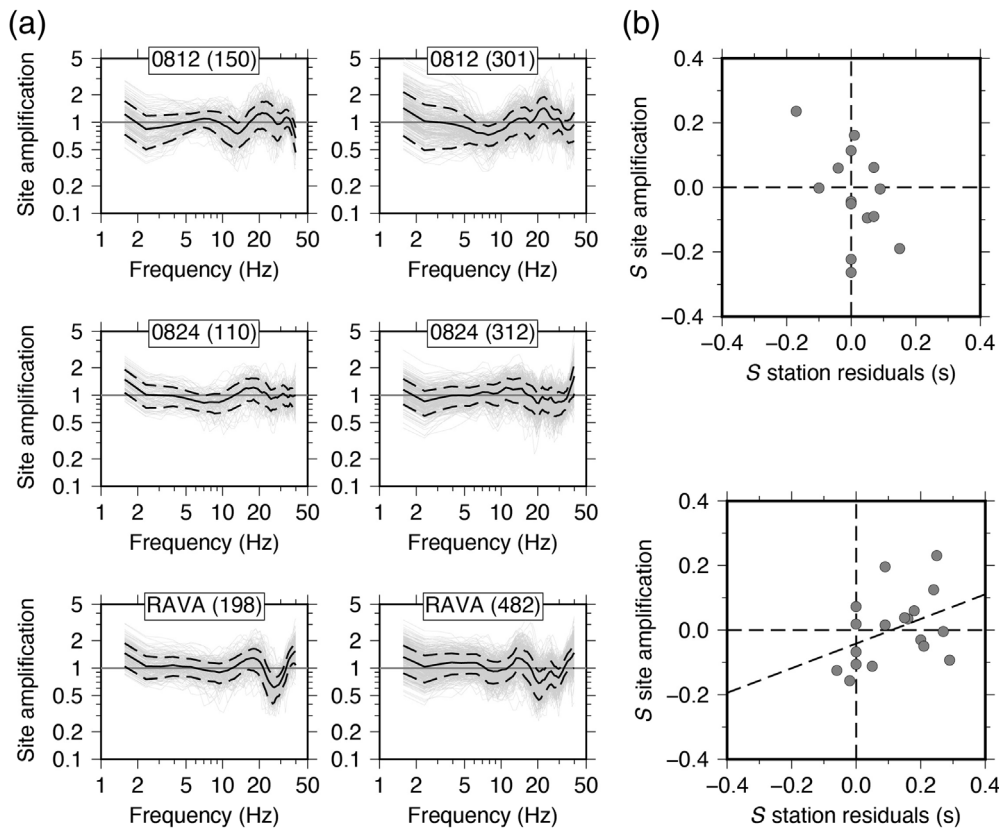
Figure 2. (a) Site responses for *P* and *S* spectra fits for the representative stations 0812, 0824, and RAVA. The first two stations are temporary, whereas the last one is permanent. Gray lines indicate individual response functions, counted by the number reported close to the station's name. The black lines indicate the mean site response function, whereas dotted lines indicate the associated error quantified by one standard deviation. (b) *P* and *S* stations residuals, resulting from the 3D velocity inversion of Pezzo *et al.* (2018), against the mean value of site response in the frequency interval 10–20 Hz. On the upper panel, we observe that station residuals from *P* model and site response are characterized by a chaotic disposition of data points; conversely, on the lower panel, for *S* waves, we observe that station residuals and site response exhibit a weak positive correlation, as evidenced by the straight-line fit of the data (black dashed line in the lower panel), having a slope of 0.38 and a coefficient of linear regression of 0.40.

recording site. Although below 10 Hz the site responses do not show large variations, and the trends are almost confined around 1.0 Hz, at higher frequencies (>10 Hz) we observe larger fluctuations with peaks between 10 and 20 Hz. Assuming a mean velocity of 3 and 1.6 km/s for *P* and *S* waves at shallow depths (Chiarabba *et al.*, 2014; Pezzo *et al.*, 2018), these frequencies are compatible with wavelengths of a few hundred meters. Therefore, the observed large amplification effects are related to small-scale complexities located at very shallow depths beneath the recording sites. Although the detailed interpretation of site responses is beyond the scope of this article, we try to explain these observations. If we correlate the mean amplitude of site response observed between 10 and 20 Hz with station residuals obtained by travel-time tomography by Pezzo *et al.* (2018) (Fig. 2b), we observe that, although *P*-station residuals do not show any apparent correlation with site responses, *S*-station residuals exhibit a weak positive correlation. This evidence suggests that the 10–20 Hz peaks of site response are related to
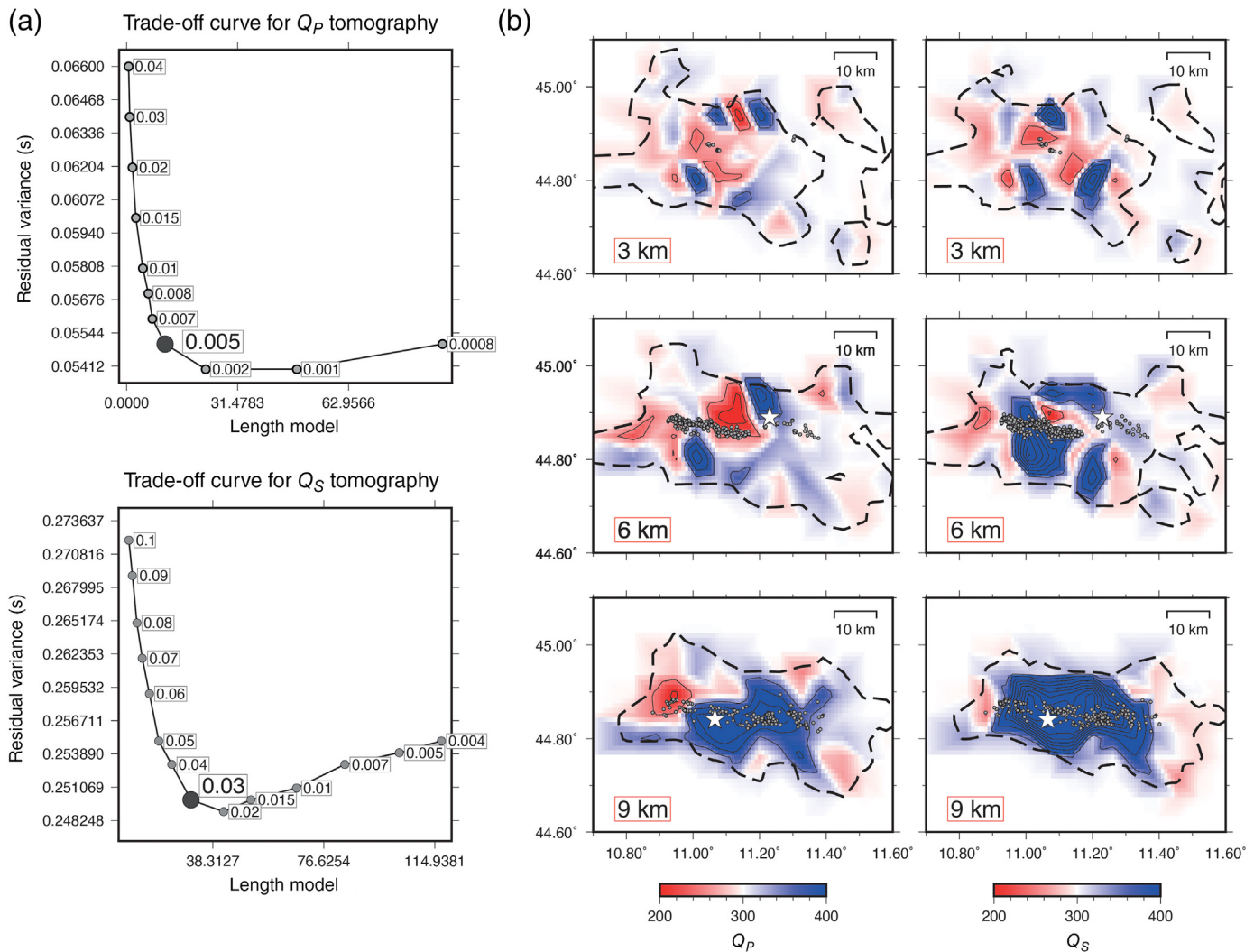
model of Pezzo *et al.* (2018).

The uniform initial Q_P and Q_S value is selected by a grid-search approach. We minimize the rms of residuals computed with the observed t^* and the synthetic ones that we obtain by tracing all seismic rays through the model, in which 3D velocity distribution and trial uniform Q values are defined (Rietbrock, 2001). The minimization of rms leads to a uniform Q_P and Q_S values of 300 as starting values for tomography. We select the optimal damping for the inversion according to the trade-off curves between model complexity and data misfit (see Fig. 3a).

For 3D inversions, Q_P and Q_S adjustments are computed only for nodes intersected by more than 10 rays. After five iterations, the final rms is 0.005 (variance improvement around 49%) and 0.007 (variance improvement of 80%) for Q_P and Q_S inversion, respectively.

The model resolution is quantified by computing the spread function (SF; Michelini and McEvilly, 1991). Following the method of Toomey and Foulger (1989), we select SF = 3 as

shallow volumes, in which *S* waves are slowed, probably due to the thicker soil coverage. It is important to remark that site responses act as a site transfer function in steps 02 and 03 of workflow. The use of site correction improves the spectral fit of *P*- and *S*-wave spectra, decreasing the final rms of about 10% with respect to a starting fit without the application of the site response correction.

Step 02: Results (tomo *Q*)

For the tomographic inversion, we use the results of spectral fit of step 02. We select only those events with at least four usable t^*, resulting in a total of 5021 t^* (from 526 events) and 8079 t^* (from 940 events) for Q_S and Q_P inversion, respectively. For both the earthquake locations and grid spacing, we mirror the tomographic model of Pezzo *et al.* (2018) that acts, in this study, as a priori information. We use nodes spaced 5 km in horizontal directions and 3 km along depth. For each node, we assign a starting value for Q_P and Q_S in addition to the 3D velocity estimates (V_P, V_S) derived from the tomographic

Figure 3. (a) Trade-off curves used to select the damping parameters for the inversions of Q_P (top) and Q_S (bottom) tomographic models. On both the curves, the bigger black dot indicates the chosen damping value. (b) Q_P and Q_S models at horizontal slices located at 3, 6, and 9 km depth. This depth interval hosts the main seismogenic volume of the sequence. The strong heterogeneities of Q_P and Q_S crustal structure result in very different attenuation terms used to correct the observed spectra before the computation of source parameters. The black dashed lines show the well-resolved region of the model with spread function < 3, as defined by Michelini and McEvilly (1991) (see also Toomey and Foulger, 1989). White stars indicate the first and the second mainshocks in the layers at 6 and 9 km depth, respectively (M_L 5.9, 20 May 2012, 02:03 UTC; M_L 5.8, 29 May 2012, 07:00 UTC); the gray dots are the aftershocks. The color version of this figure is available only in the electronic edition.

a reliable threshold below which Q_P and Q_S nodes are characterized by a satisfactory ray sampling and compact averaging vector (i.e., vectors picked on their diagonal values).

Again, because a detailed interpretation of the 3D attenuation tomography results is beyond the scope of this article, we limit our description to the main features at significant depths (Fig. 3b). Both Q_P and Q_S models show nearly checkerboard patterns of relatively high (lower attenuation, blue areas) and low values (higher attenuation, red areas) at shallow depths (0–3 km), reflecting the complexity of the attenuation structure in the sedimentary cover and at very local scale. At intermediate depths (around 6 km) the attenuation pattern shows a prevalence of higher values (Q_S up to 400, lower absorption) in the central part of the Q_S model, whereas the Q_P structure is more complex, with a prevalence of relatively high attenuation (Q_P down to 200) in its central part. It is noteworthy that the bulk of earthquakes at this depth (including the first mainshock, white stars in Fig. 3b) occurs at the boundary between relatively higher and lower attenuation volumes, both in the Q_P and in the Q_S models. Finally, at greater depths (around 9 km), a broad relatively low attenuation characterizes both the Q_P and Q_S models.

Here, high Q_P and Q_S (both up to 400) volumes contain the seismicity, including the second mainshock (white stars at 9 km depth in Fig. 3b).

Step 03: Results (source parameters)
At the end of step 03 of workflow, all the usable spectra are corrected for attenuation by means of 3D attenuation tomography.
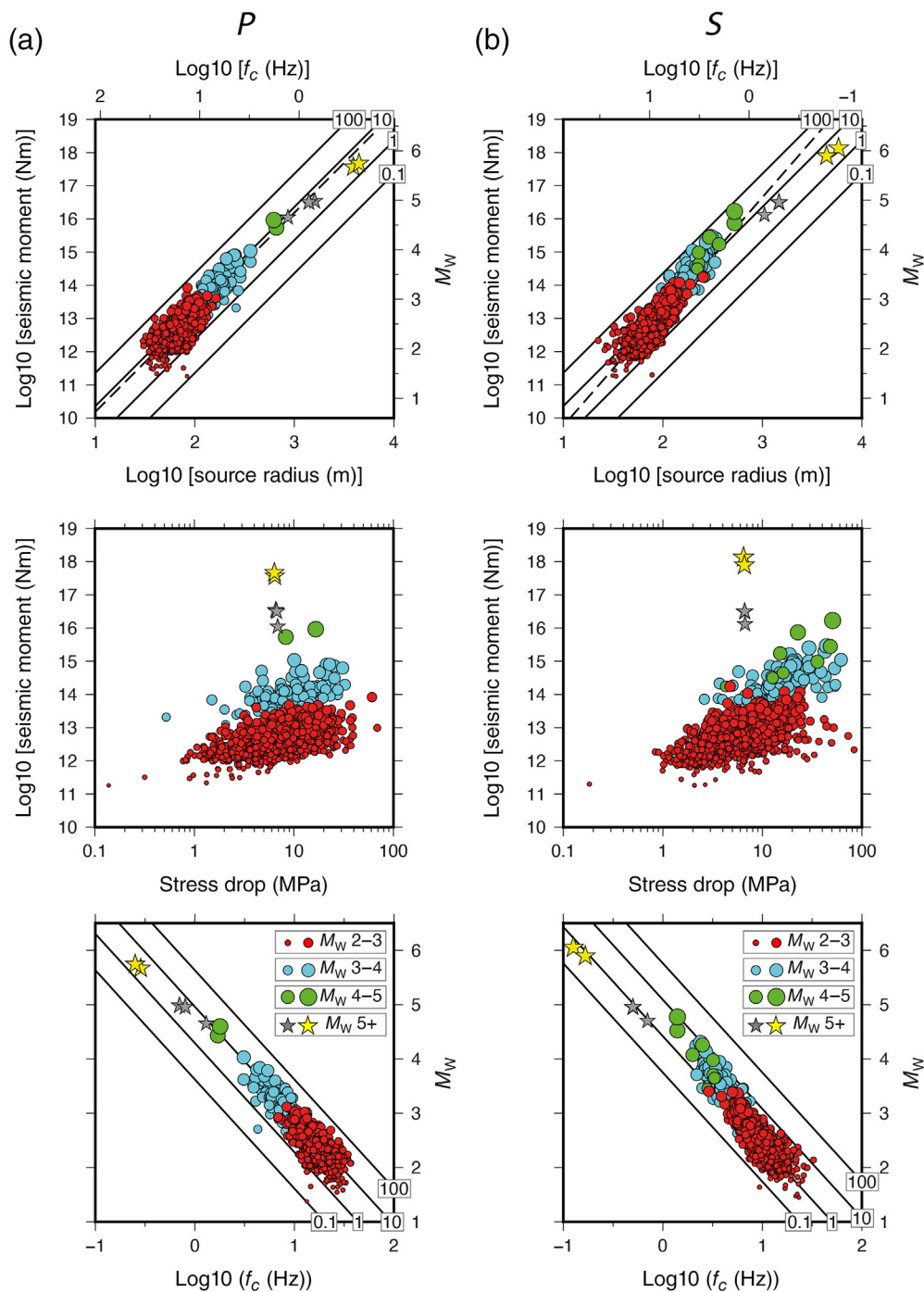
Figure 4. Source parameters determined from the fit of (a) *P* and (b) *S* spectra. For each phase, the seismic moment versus source radius (top), seismic moment versus stress drop (middle), and moment magnitude versus corner frequency (bottom) are reported. Aftershocks are drawn by circles sized and colored on the basis of their magnitude according to the legend on the bottom panels. Stars are **M** 5+ events. On the upper and bottom panels, black lines refer to constant stress-drop values expressed in MPa. The color version of this figure is available only in the electronic edition.

selection criterion reduces the number of available events for source-parameter computation but provides the best fit for robust computations of source parameters.

We now consider the application of classical equations (5)–(7) for the computations of the static source parameters. Errors on source-parameter estimation are discussed in the next section.

From the event source corner frequency, we compute the source dimension (r) by applying equation (6). Because we have one value of f_c for each event, the seismic radius is not averaged among the stations of the events, but it is simply a single value. The estimation of the event seismic moment is performed averaging the contribution of each station. For each estimate of the low-frequency level (Ω_0), we apply equation (5) using $V_S = 3.5$ km/s as average velocity of the seismic volume (Pezzo *et al.*, 2018) and a crustal density of 2800 kg/m^3. For the geometrical spreading that enters in equation (5), because our dataset consists of earthquakes recorded at short epicentral distance, the simple 1/D function is a valid assumption (Edwards *et al.*, 2008; de Lorenzo *et al.*, 2010). From the estimation of seismic moment, we compute the moment magnitude (M_w) through the relationship (Hanks and Kanamori, 1979):
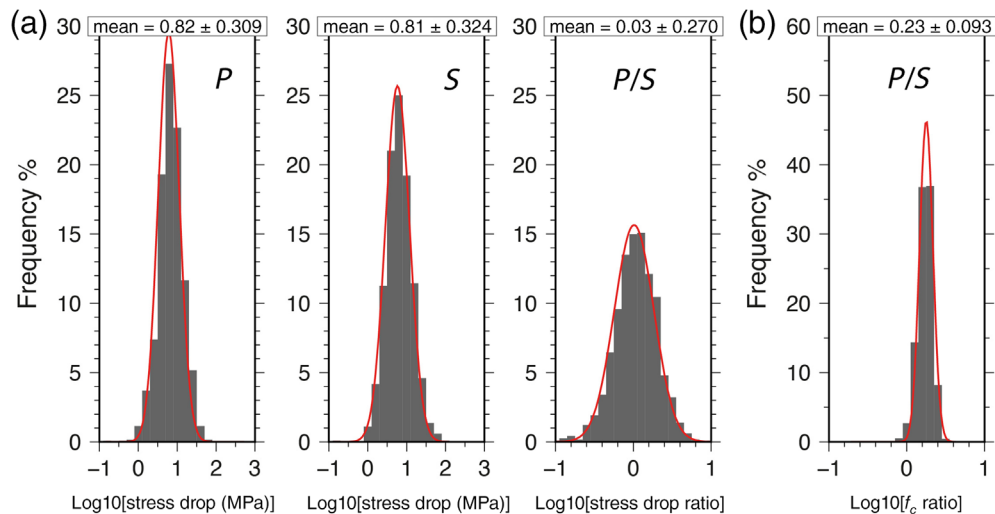
$$M_w = \frac{2(\log M_0 - 9.1)}{3}, \quad (14)$$

in which M_0 is the seismic moment expressed in Nm.

M_0 and source dimensions are subsequently used in equation (7) to calculate the released stress drop.

In Figure 4, we present the results of the static source parameters obtained by the *P*- and *S*-wave spectra (from

For each event, we estimate a common source corner frequency and single-station low-frequency levels. Based on the quality of spectral fitting (Eberhart-Phillips and Chadwick, 2002), we retain all the events with at least four spectra with fit quality of 0, 1, and 2, discarding the worst fit with weight >2. This

Figure 5. (a) Histograms showing the frequency distribution of *P* stress drop (left), *S* stress drop (middle), and of the ratio between *P*- and *S*-wave stress drops (right). On the top of each histogram, the mean and the standard deviation of the log-normal distribution are reported. (b) Histogram of the ratio between the *P* and the *S* source corner frequency. In log space, the average ratio is 0.23 ± 0.09 that leads to a mean ($f_c P / f_c S$) of 1.70 with a confidence interval between 1.37 and 2.10. The color version of this figure is available only in the electronic edition.

1207 and 1171 events, respectively) by three different bi-dimensional plots. We show the variation of seismic moment versus the source dimension (Fig. 4, top panel) and released stress drop (Fig. 4, middle panel), In addition, we report the distribution of the source corner frequency against the moment magnitude (bottom panel in Fig. 4). On the first and last plots, we superimpose the black lines that delineate the values of constant stress drop. All the aftershocks processed by the described procedure are represented in Figure 4 by circles with size and color depending on the magnitude (according to the legend on the bottom panels). Stars are the events with magnitude greater than 5, including the two mainshocks, that we have treated separately, without the use of tomo *Q*, that are included to realize a complete analysis of the source parameters of the study sequence. At the end of our multistep procedure, we obtain the estimates of the static source parameters for a total of 1240 aftershocks.

As a general observation, we observe that source parameters computed using *P*- and *S*-wave spectra give similar results. Our data show that seismic moments span over about five orders of magnitude, from 10^{11} to 10^{16} Nm, whereas seismic radii are in the range of 30–650 m. The seismic moment and the source dimension show approximately a linear trend. Although points are bound by lines of constant stress drop that cover two orders of magnitudes, these observations are compatible with the earthquake scaling of constant stress drop, as widely reported in many studies worldwide (see Abercrombie, 2021). In our case, stress drops of aftershocks are mostly confined between 1 and 100 Mpa. The log-space mean value of the aftershock stress drop is displayed by histograms of Figure 5a. *P*- and *S*-wave analysis gives similar results: The average stress drop is of about 6.7 Mpa

for *P* and *S* waves, with a ratio of 1.07. The largest events, with stress drop ranging from 1 to 10 Mpa, are in agreement with the aftershocks averaging values and exhibit source dimensions coherent with a linear trend (Fig. 4, top and bottom panels).

The corner frequencies are mostly in the range 3–30 and 2–25 Hz for *P* and *S* waves, respectively (Fig. 4, top and bottom panels). The ratio between $f_c P$ and $f_c S$, estimated from the log-normal histogram, is 1.70 (see Fig. 5b). Because the log-space standard deviation is 0.09, the confidence limits of mean ratio are between 1.37 and 2.10, which is a variability that includes the theoretical estimates of 1.5 based on the circular rupture model (Madariaga, 1976).

We also compare the moment magnitude M_w determined with *P* and *S* spectra with the local magnitude determined by the Istituto Nazionale di Geofisica e Vulcanologia (INGV) analysts (ISIDe Working Group, 2007). Even if for M_L smaller than about 2.5–3.0, we observe a larger scatter of data; the scatter plot of the M_w versus M_L is fairly well represented by a 1:1 relation for all the magnitude range, both for *P*- and *S*-wave data (Fig. 6).

We fit our M_L–M_w data by an orthogonal regression that minimizes the Euclidean distance between each data point and the fitting line (Golub and Van Loan, 1980). This approach should be preferred to the standard regression strategies when data are affected by unknown uncertainties (in our pool of data, this is the case of M_L; see Di Bona, 2016). To compute the error on the slope and the intercept, we apply the bootstrap method with 1000 resamples of the original data distribution computing a regression for each realization (Fig. 6). For each fitting line, the slope and its error, as well as the intercept and its standard error, are reported in Figure 6.

The self-similarity of earthquakes

Earthquakes are defined as self-similar when the released stress drop is constant. This means that the event magnitude and the surface rupture increase or decrease according to equation (7). From equation (7), taking the logarithms, we can write

$$\log 10(M_0) = \log 10(2.2857\Delta\sigma) + 3\log 10(r). \qquad (15)$$

Reporting in a 2D plot the seismic moment as a function of the fault dimension (as in the top panels of Fig. 4) for the
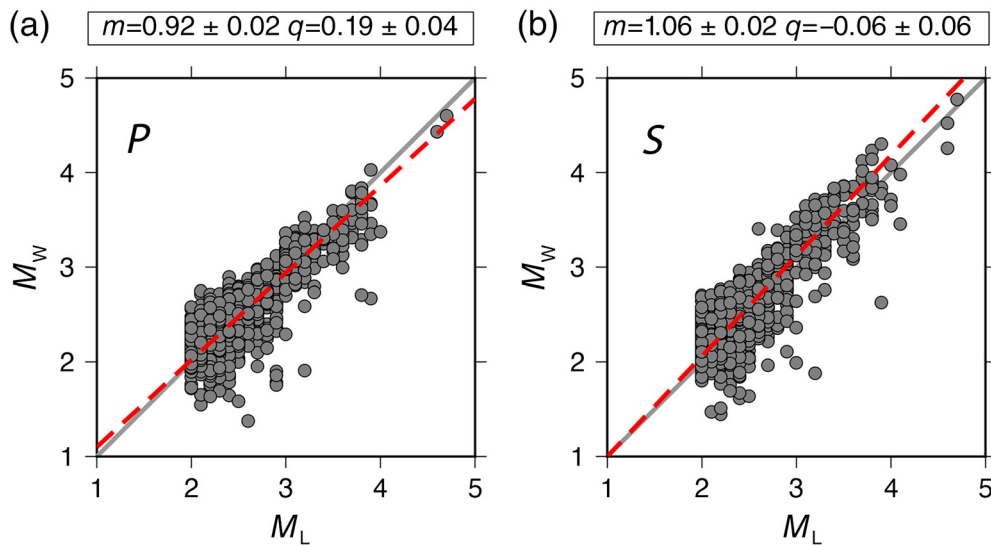
Figure 6. Local (M_L) against the moment magnitude (M_w) deriving from (a) *P*- and (b) *S*-wave spectra fit. The gray lines indicate $M_L = M_w$. The dashed lines are the results of the orthogonal regression of our M_L–M_w data performed minimizing the distance between each data point and the resulting line. This approach should be preferred to the standard regression strategies, when data are affected by unknown uncertainties (in our pool of data, this is the case of M_L; Golub and Van Loan, 1980). In the title of each plot, we report the details of the fitting line: the slope (*m*), its error as well as the intercept (*q*), and its uncertainty. The color version of this figure is available only in the electronic edition.

(see equations 6 and 7), and the error on f_c propagates heavily on the uncertainty of stress drop (see equations 6–8).

For example, assuming an *S*-wave spectrum characterized by a low-frequency level Ω_0 of 1×10^{-6} and $f_c = 10$ Hz with 1 Hz of standard deviation (relative error of 10%), the stress-drop value ranges approximately from 10 to 18 Mpa, if other sources of errors are neglected. If the standard deviation is of 2 Hz (relative error of 20%), stress drop could vary between 7 and 24 Mpa. The same calculation carried out at $f_c = 20$ Hz gives larger stress-drop variations with values from 80 to 150 Mpa.

A wide variability of stress-drop error is reported in the literature. For example, Cotton *et al.* (2013) state that the approaches that rely on spectral determination of seismic moment and corner frequencies lead to large scatter in stress-drop determination and to large uncertainties in predicting seismic hazard. In our case, we are confident that correcting spectra for tomo *Q* give reliable f_c determination and robust stress-drop determinations.

For each event, and for each step of our procedure, we compute accurately the error on f_c using two independent approaches. When both the methods provide similar error estimates, we are confident that the fitting approach is giving robust results, and the final fit is retained. Conversely, when the two methods give different estimation of f_c error, the final fit is discarded.

First, we quickly estimate the f_c uncertainty by means of the second derivative of the MF curve around its minimum (Menke, 2018). It follows that the f_c error is strongly dependent on the shape of the MF. When the MF curve is characterized by a well-picked minimum, the f_c error is small, conversely an almost flat MF leads to ambiguous f_c and to large error estimates.

To strengthen the evaluation of errors about f_c (for *P*- and *S*-wave spectra), we furtherly applied, for each event, a method based on a bootstrap approach described in YEA for coda spectra. Once the event f_c and single stations Ω_0 and t^* have been defined by MF analysis, we computed the residuals between observed and theoretical amplitudes. To create a bootstrap sample, we randomly take values from residuals dataset allowing the selection of a single value more than once. This is the "replacement" process of bootstrap statistics

analyzed dataset, if the self-similar trend is respected, the events should define a straight line with slope equal to 3 and an intercept that is function of the constant stress-drop value.

To verify if our dataset is in agreement with the self-similar model, we fit the *P*- and *S*-wave datasets with a free straight line (dashed lines in top panels of Fig. 4) and with equation (15), in which the slope is fixed to 3. The corrected Akaike criterion is applied to understand whether the constant stress-drop model is better, in a statistical sense, than the case in which stress drop increases with source dimensions. For *P*-wave data (Fig. 4a), the modified Akaike criterion indicates that fitting line with slope fixed to 3 is significantly better, in a statistical sense, than the free straight-line, suggesting a self-similar behavior. For *S*-wave data (Fig. 4b), the same statistical test strongly supports the fitting line, for which slope is greater than 3 (slope = 3.443), suggesting that stress drop is proportional to source dimension, therefore violating the self-similarity concept.

The breakdown of earthquake self-similar scaling, as seen through *S*-wave analysis, has been observed in quite a few studies on single seismic sequences (e.g., Pacor *et al.*, 2016; Wang *et al.*, 2019; and references therein). In our case, the fact that *P*-wave data show a self-similar behavior differently to what the *S* waves suggest leads to an apparent incongruence that deserves further specific studies.

Error analysis on source-parameter estimation

The crucial point for studies focused on the determination of source parameters is the estimation of f_c and its uncertainties. Stress drop, in fact, is proportional to the cubes of f_c

(Efron, 1979). The resampled values are then summed to the theoretical amplitudes to obtain the simulated spectra of the event. These spectra are then fitted as in the real case to find the event f_c and single stations Ω_0 and t^*. For each event, we perform 1000 bootstrap realizations, thus collecting 1000 values of f_c from which we construct a histogram that describes the sampling distribution from which we compute the mean f_c and its standard error. The f_c characteristics (mean and standard deviation) bootstrap-derived are then compared with those derived by the MF curve. When both the methods provide similar f_c and related error estimates, we are confident that spectral fits are robust, and the subsequent estimation of source parameters are reliable. Conversely, a disagreement between MF and bootstrap resampling outcomes suggest that the final fit is poorly constrained, and it should be discarded. After a visual inspection of results, we decided that, for an event to be retained, the maximum threshold between MF and bootstrap results should be within 1.5 Hz.

In Figures 7 and 8, we show, for representative small-magnitude event (in the range 2–3), the MF curve and the histogram of the bootstrap resampling for P- and S-wave spectral fitting, respectively, in the first and last part of the workflow (steps 01 and 03, see Table 2). At the beginning of step 01, spectral fit are carried out with any a priori information, whereas, in step 03, we correct site effects with the site responses obtained at the end of step 01 and path attenuation with the tomographic t^* determined at the end of step 02.

Small-magnitude events (in the range M_L 2–3) are, in general, the most problematic in determining a reliable value of f_c (Klinger and Werner, 2022; Parolai and Oth, 2022). For the event of M_L 2.2 (Figs. 7 and 8 for P- and S-wave fits, respectively), in step 01, the rms versus the trial f_c, after an evident decrease of rms at very low f_c values, shows an almost flat trend at increasing f_c, describing an L-shaped curve. From a numerical point of view, the minimum exists, but it is weak, and it is visible only by zooming around the minimum itself (see gray insets in Figs. 7 and 8). This observation holds for P- and S-wave fitting run the step 01 of the workflow.

This trend is mainly due to attenuation effects that mask the source decay, and the minimum of the curve is unclear and ambiguous. Consistently, the f_c distribution bootstrap-derived is characterized by an irregular shape with a mean value and a standard deviation very distant from the value obtained by the MF curve (Figs. 7a and 8a, for P and S spectral fits, respectively). The disagreement between MF and bootstrap-derived estimations is the proof that the spectral fit is unconstrained. In this case, we skip the P and the S spectral fits, and this event (M_L 2.2 in Figs. 7 and 8) does not contribute to the estimation of site response and of attenuation seismic tomography. After the visualization of results, we decided that the maximum permissible deviation between MF and bootstrap-derived estimation (of f_c and standard error) is 1.5 Hz. Above this threshold, the spectral fit is discarded.

The main important aspect is that, when the same event is processed using site response and t^* fixed as a priori information, the attenuation effect is decoupled from the source spectral decay, and the search for the event corner frequency is strongly improved (Figs. 7b and 8b, for P and S spectral fit, respectively).

As it is clearly observable in Figures 7b and 8b, the rms versus f_c is now picked on a well-defined minimum. The bootstrap-derived distribution shows that the mean f_c and its standard deviation are almost identical to the values extracted by the MF curve.

This coherence allows us to select the event previously discarded for P and S source-parameter computation. In this range of magnitude (2–3), the introduction of synthetic t^* lead to well-constrained fit with a remarkable increase of the number of spectra usable for source-parameter estimation (see numbers enclosed in parentheses in Table 1). For S waves, the number of events increases by about 30% with respect to the events used for tomography. For P waves, this increment is even greater, because fewer events are input for tomographic inversion.

At greater magnitudes (classes M_L 3–4 and 4–5), the improvement generated by the tomography is less pronounced, being the number of events almost similar at each step of the workflow (see the supplemental material for the description of the MF curves and the histograms for events of greater magnitudes classes). For $M_L > 3$, in fact, the MF curve and bootstrap-derived distribution are well defined at each step. The corner frequency is well constrained by a well-defined minimum, and the estimated errors are similar (see Figs. S5–S6 and S7–S8 for events of M_L 3.9 and M_L 4.4, respectively). We stress that using tomo Q to correct spectra, the final fit is sensibly improved, because the minimum of MF curve is found for rms values lower with respect to the starting fit.

In addition to the f_c, the uncertainties of the other source parameters are computed as follows. At the end of step 03 of workflow, all the usable spectra are corrected for attenuation by means of 3D attenuation tomography. For each event, we estimate a common source corner frequency and single-station low-frequency levels. From the source corner frequency, we compute the source dimension (r) by applying equation (6); its error, σ_r, is related to the error on f_c estimate (σ_{f_c}) by the relation:
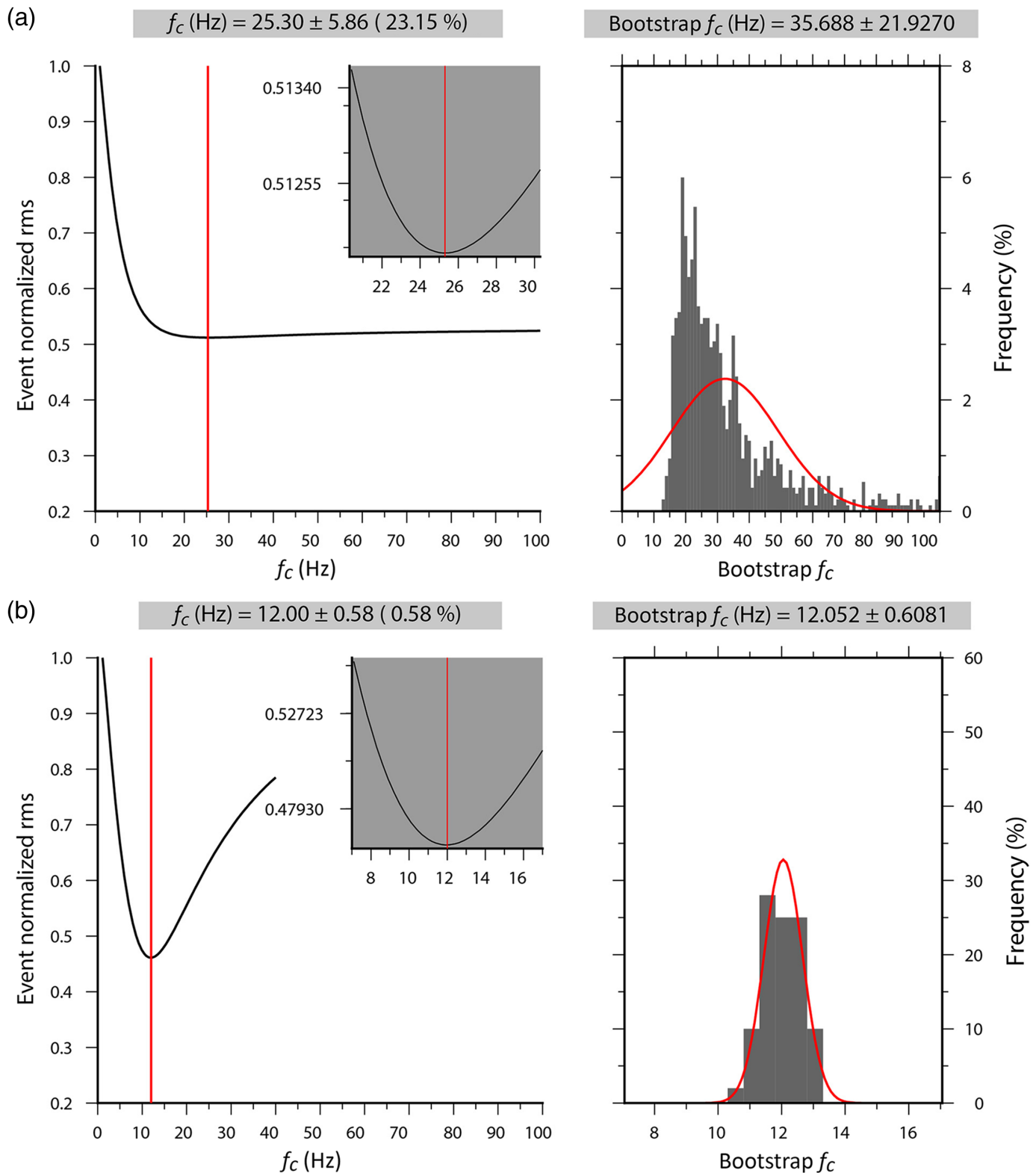
$$\frac{\sigma_r}{r} = \frac{\sigma_{f_c}}{f_c}. \tag{16}$$

For the estimation of the seismic moment, we average the contribution of all the available stations. Because the fitting procedure furnishes the low-frequency level and the rms for each spectrum, we apply equation (5) for each station, and we compute the mean seismic moment and its uncertainty under the assumption that data are log-normally distributed (Archuleta et al., 1982; Fletcher et al., 1984). In particular, we apply a weighted mean in log space in which the fit rms acts as the inverse of the weight for the station seismic moment. The standard deviation of the mean that represents
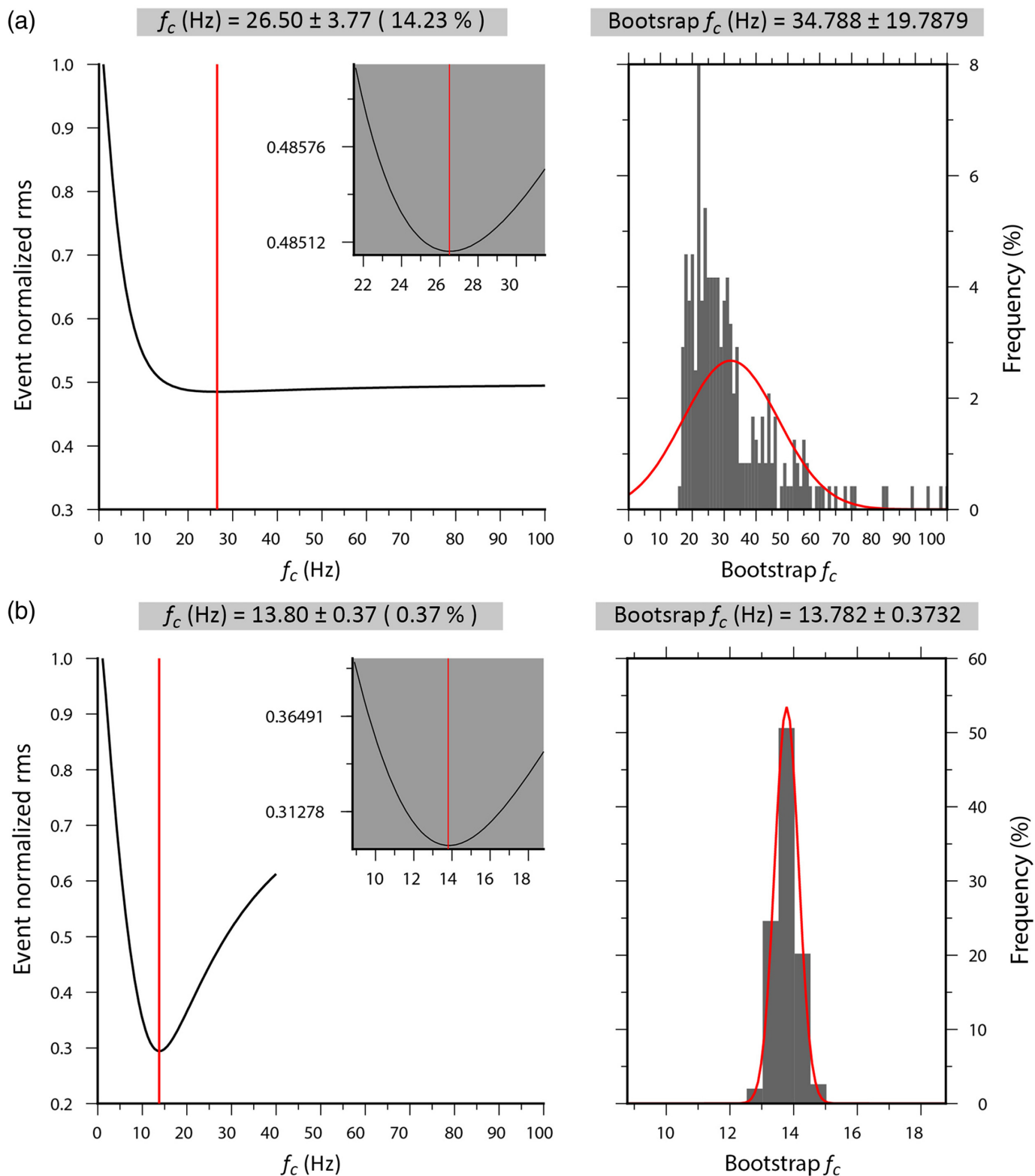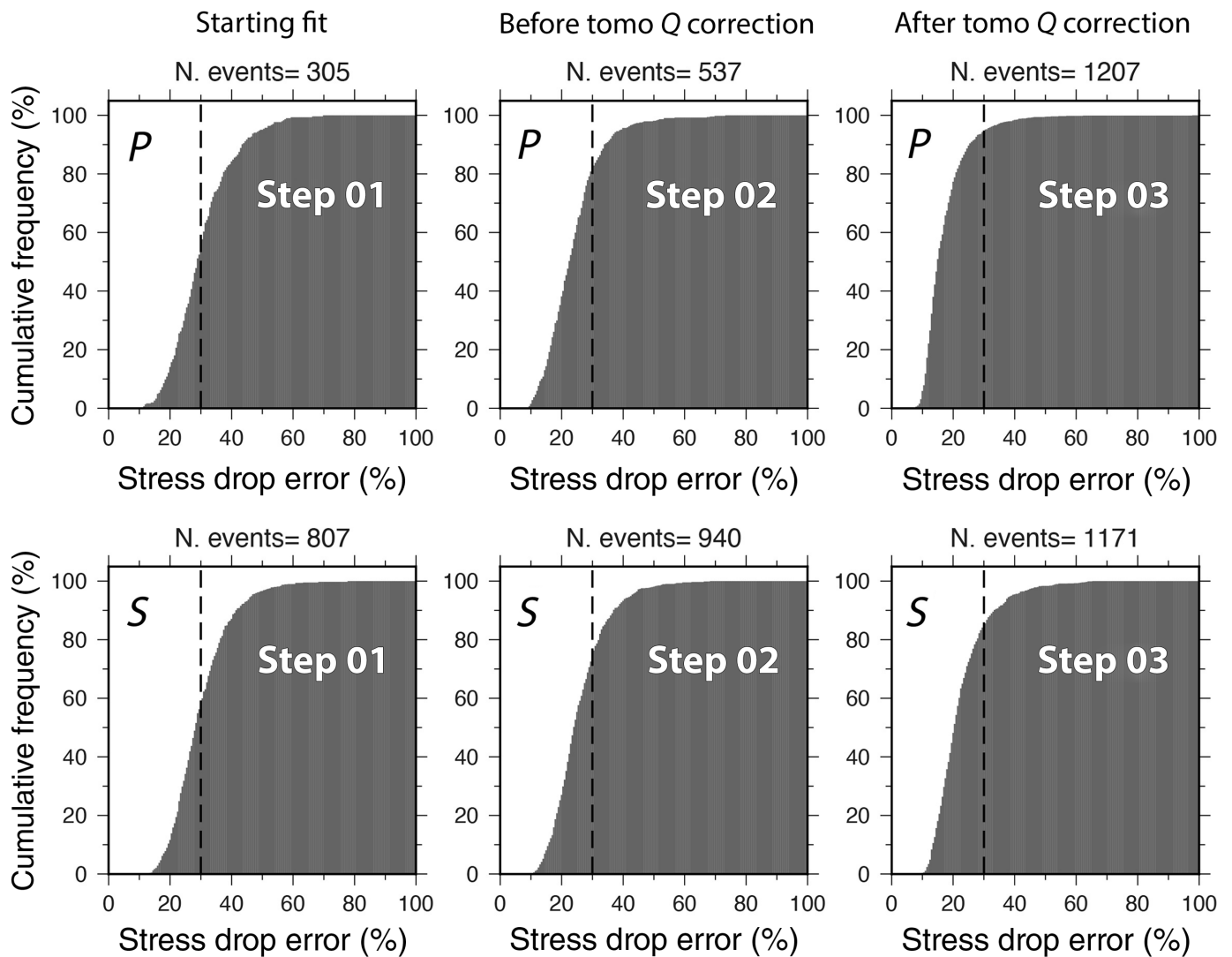
Figure 7. Misfit function (MF) deriving from the P–f_c grid search of one event of M_L 2.2; In both (a) and (b) panels, the gray inset shows a zoom around the minimum (left); histogram of the bootstrap resampling shows the distribution of the recovered f_c (right). Titles on the left plots report the final value of f_c with its absolute and relative error, whereas, on the right, the f_c along with the associated standard deviation deduced by the bootstrap histogram is indicated. In panel (a), spectra are processed with any a priori assumptions (step 01 of the workflow), whereas spectral fits are carried out fixing the spectral attenuation to the values extracted by the 3D Q model in panel (b). It is noteworthy that we could not identify a clear minimum of the MF in panel (a), although the inset show that it numerically exists; the bootstrap histogram is also irregular showing a blurred f_c distribution; we observe a well-picked minimum in the misfit curve and well-shaped frequency distribution of the bootstrap f_c in panel (b). The color version of this figure is available only in the electronic edition.

Figure 8. (a,b) MF deriving from the S–f_c grid search of the same event of M_L 2.2 of Figure 7; see other details in the caption of Figure 7. The color version of this figure is available only in the electronic edition.

the error bar in the logarithmic plot related to the seismic moment is then converted into the multiplicative factor defined by Fletcher *et al.* (1984) that enters in equation (8) for the estimation of stress-drop error. In this work, the multiplicative factors are in the interval ranging from 0.04 to 0.97 for both P and S spectra, a range of values coherent with those reported in table 2 of Fletcher *et al.* (1984).

Figure 9. Cumulative histograms showing the distribution of stress-drop relative errors as obtained for *P*- (upper panels) and *S*-wave (lower panels) spectral fit. Left and central panels refer to errors computed in the steps 01 and 02 of the workflow, respectively. On the right panels, errors are related to spectral fit, in which *Q* tomography (tomo *Q*) is used to correct attenuation. As title, the total number of events is reported. In each panel, the dashed vertical line indicates the 30% of the stress-drop error values. Using tomo *Q*, we get final stress-drop errors within 30% for the 80% of the events, and the number of usable events for source-parameter consideration is sensibly higher.

The released stress drop and its error are computed by applying equations (7) and (8), respectively.

In Figure 9, we show the relative uncertainty of stress drop for *P* and *S* waves compared to the same estimation obtainable in steps 01 and 02 of the workflow, without correcting spectra for tomographic attenuation. About 80% of stress-drop estimations are characterized by relative error within 20% with maximum values of about 40% (Fig. 9, right-upper and -lower panels, for *P* and *S* spectral fits, respectively). It is worth seeing that without the contribution of tomo *Q* (steps 01 and 02 of the workflow) the number of acceptable fits is sensibly lower and the error quality on stress-drop estimation decreases for both *P* and *S* spectral fits (Fig. 9, middle and left panels, for steps 02 and 01, respectively).

Kane *et al.* (2011), using a frequency domain EGF approach, estimated that the minimum error related to stress-drop estimation should be of about 30%. In our approach, at step 02 of the workflow, for the 80% of events, errors are mostly around 30% with a few percent of events with error between 30% and 40% (Fig. 9, middle-upper and -lower panels, for *P* and *S*

spectral fits, respectively). Our results are, on average, coherent with the conclusion of Kane *et al.* (2011). The spectral correction using tomo *Q*, however, leads to an improvement (Fig. 9, right-upper and -lower panels, for *P* and *S* spectral fits, respectively). For the common events processed in the three steps of the workflow (299 events for *P* and 837 for *S* waves), we observe that the final reduction of the stress-drop uncertainty is, on average, of 48% and 32% for *P* and *S* spectral fits, respectively.
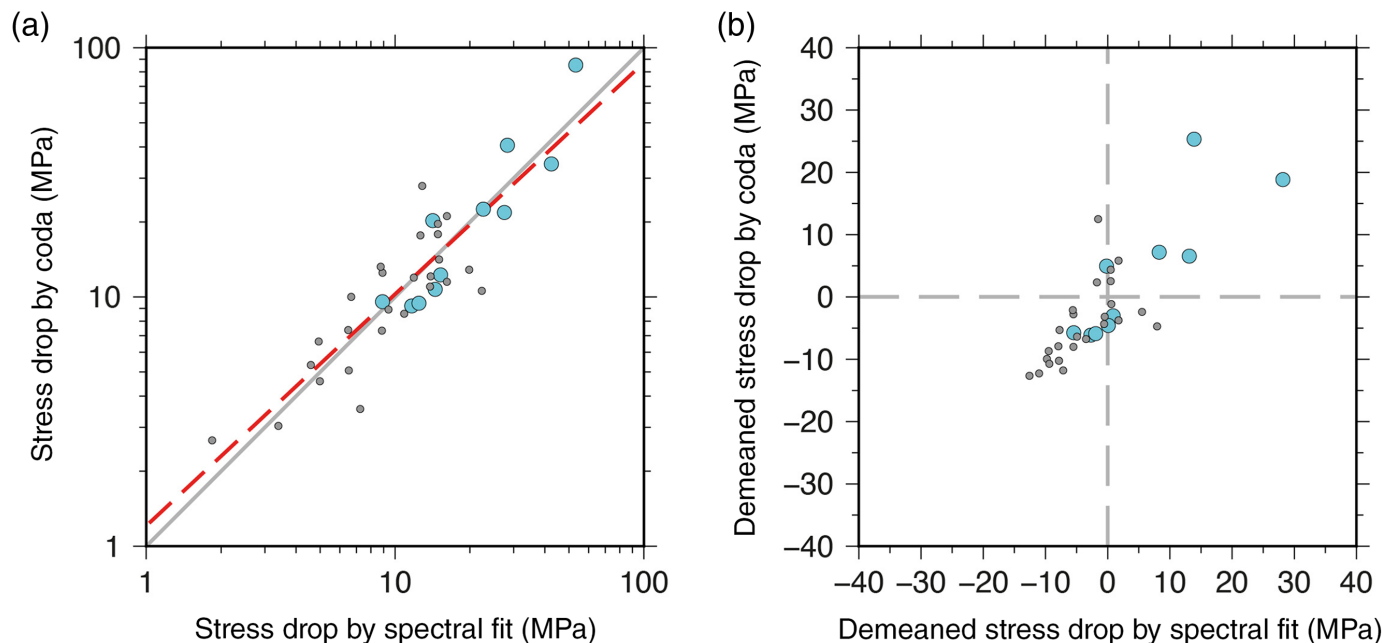
Because errors on stress drop are dominated by uncertainty of f_c, we are confident that our results benefit from the small error on f_c determination.

COMPARISON OF STRESS-DROP ESTIMATIONS BY DIRECT *S*- AND CODA-WAVE FITS

To better assess the performance of our method and to critically evaluate the results, we compare our *S*-wave f_c estimations with those derived by applying the method of YEA, in which coda-wave spectral ratios are used. We focus our comparison with the YEA method because the estimation of f_c relies on seismic waves (coda waves) independent from the *S* body waves used in the spectral inversion scheme proposed. The methodology used for this comparison is fully described in the supplemental material. For the sake of brevity, here, we only show the results of the comparison between the two approaches. In Figure 10, stress-drop values determined through the YEA method are compared with stress drop estimated by the spectral fit procedure. We observe that the points lay on the proximity of the equal-value line (gray line in Fig. 10a), showing a substantial agreement between the stress-drop values determined by the two independent methods, as matter of fact, the computed linear regression of the data points (red dashed lines in Fig. 10a) is characterized by a slope being very close to 1.

If we compare the stress-drop variations computed with respect to the average value for the same pool of data, we observe that the majority of points fall in the northeast–southwest quadrants, delineating a positive correlation between stress-drop variations. Because the average stress-drop value is determined separately for coda and spectral fit data, this plot demonstrates that both the stress-drop datasets give equivalent indications about the variability of stress drop with respect to the mean value (Fig. 10b)

Figure 10. Comparison of stress drop computed by spectral fit and coda-wave approach. Larger circles represent the master events of each cluster (all in the magnitude interval 3–4). Each small gray point represents empirical Green function belonging to at least two clusters. (a) Comparison between absolute values of stress drop. The gray line indicates equal values of stress drop. The dashed line represents the linear fit of data: slope = 0.87, intercept = 1.05. (b) Comparison of stress-drop variation with respect to the mean value using the same datasets of panel (a). Gray-dashed lines indicate null variations with respect to the average stress drop. The color version of this figure is available only in the electronic edition.

CONCLUSIONS

We computed the source parameters for 1240 aftershocks of the 2012 Emilia sequence (1207 from *P* waves and 1171 from *S* waves, respectively; 1138 events have estimates from both *P* and *S* waves), with magnitude ranging from 2.0 to 4.7 by applying two independent methods. First, we use a classical approach based on the spectral fit of *P*- and *S*-wave body waves to a dataset of 1306 seismic events with $M_L \geq 2$. We corrected the attenuation by means of a 3D Q_P and Q_S tomographic model computed using the same dataset starting from tomographic models (V_P, V_S) and 3D locations used as a priori information. The results deriving either from *P*- and *S*-wave spectral fit are coherent and give similar estimates of source parameters. Seismic moments are in the range 10^{11}–10^{16} Nm, and stress-drop values range from 0.1 to 83 Mpa, whereas the variability of source dimensions is in the interval 30–650 m. *P*-wave spectral fit gives seismic moment and source dimensions that scale in a self-similar model with an almost constant stress drop of 6.7 Mpa. Conversely, we obtain a proportionality between stress drop and source dimension for *S* waves, suggesting a violation of self-similarity, as observed for other seismic sequences (e.g., Malagnini *et al.*, 2008; Pacor *et al.*, 2016;

Wang *et al.*, 2019; and references therein). The fit of seismic moment versus f_c shows that $M_0 \propto f_c^{-0.3443}$.

Separately, we compute the source parameter following the procedure described in YEA based on the modeling of coda spectral ratio. Our results show that the stress-drop estimates are almost similar to that obtained for *S*-wave spectral fit. This agreement suggests that the assumptions that we choose to perform spectral fit, not required by coda spectral ratio modeling, are in general correct.

Although the method of YEA could lead to high-precision stress-drop determination for very populated clusters, the analysis conducted by spectral fit using attenuation tomography gives the opportunity to compute stress drop for a larger number of events, exploiting, for example, entire aftershock sequences. Because the aftershocks, spreading over the main rupture planes and secondary structures, reveal the geometric details of the activated faults (Valoroso *et al.*, 2012; Chiaraluce *et al.*, 2017), this approach gives the opportunity to analyze the spatial patterns of stress-drop variations, hence infers the mechanical state over the whole ruptured fault system.

DATA AND RESOURCES

The seismograms analyzed in this work are available through the European Integrated Data Archive (EIDA) web services (https://www.orfeus-eu.org/data/eida/webservices/, last accessed January 2023). Data from Istituto Nazionale di Geofisica e Vulcanologia (INGV) are available at doi: 10.13127/SD/X0FXNH7QFY. The supplemental material contains additional details on the dependency of the quality factor (*Q*) from the frequency, on the error analysis on source-parameter estimation, and on the comparison of stress-drop estimations by direct *S*- and coda-wave fits. Furthermore, it contains examples of spectral fit for lower magnitude events and of the fitting procedure in the different steps of the workflow described in this article. The figures were drawn using the Generic Mapping Tools (GMT; Wessel *et al.*, 2013) software.

DECLARATION OF COMPETING INTERESTS

The authors declare that there are no conflicts of interest.

ACKNOWLEDGMENTS

REFERENCES

Abercrombie, R. E. (1995). Earthquake source scaling relationships from -1 to 5 M L using seismograms recorded at 2.5 km depth, *J. Geophys. Res.* **100,** 24,015–24,036.

Abercrombie, R. E. (2015). Investigating uncertainties in empirical Green's function analysis of earthquake source parameters, *J. Geophys. Res.* **120,** 4263–4277, doi: 10.1002/2015JB011984.

Abercrombie, R. E. (2021). Resolution and uncertainties in estimates of earthquake stress drop and energy release, *Philos. Trans. R. Soc. Lond. A* **379,** doi: 10.1098/rsta.2020.0131.

Adams, D. A., and R. E. Abercrombie (1998). Seismic attenuation above 10 Hz in southern California from coda waves recorded in the Cajon Pass borehole, *J. Geophys. Res.* **103,** 24,257–24,270.

Aki, K. (1967). Scaling law of seismic spectrum, *J. Geophys. Res.* **72,** 1217–1231.

Allmann, B. P., and P. M. Shearer (2007). Spatial and temporal stress-drop variations in small earthquakes near Parkfield, California, *J. Geophys. Res.* **112,** no. B4, doi: 10.1029/2006JB004395.

Archuleta, R. J., E. Cranswick, C. Mueller, and P. Spudich (1982). Source parameters of the 1980 Mammoth Lakes, California, earthquake sequence, *J. Geophys. Res.* **87,** 4595–4607.

Bindi, D., R. R. Castro, G. Franceschina, L. Luzi, and F. Pacor (2004). The 1997–1998 Umbria-Marche sequence (central Italy): Source, path, and site effects estimated from strong motion data recorded in the epicentral area, *J. Geophys. Res.* **109,** no. B4, doi: 10.1029/2003JB002857.

Boatwright, J., J. B. Fletcher, and T. E. Fumal (1991). A general inversion scheme for source, site and propagation characteristics using multiply recorded sets of moderate-sized earthquakes, *Bull. Seismol. Soc. Am.* **81,** 1754–1782.

Boore, D. M. (1983). Stochastic simulation of high-frequency ground motions based on seismological models of the radiated spectra, *Bull. Seismol. Soc. Am.* **73,** 1865–1894.

Boore, D. M., and J. Boatwright (1984). Average body-wave radiation coefficients, *Bull. Seismol. Soc. Am.* **74,** 1615–1621.

Brune, J. N. (1970). Tectonic stress and the spectra of seismic shear waves from earthquakes, *J. Geophys. Res.* **75,** 4997–5009.

Chiarabba, C., P. De Gori, L. Improta, F. P. Lucente, M. Moretti, A. Govoni, and A. Nardi (2014). Frontal compression along the Apennines thrust system: The Emilia 2012 example from seismicity to crustal structure, *J. Geodynam.* **82,** 98–109, doi: 10.1016/j.jog.2014.09.003.

Chiaraluce, L., R. Di Stefano, E. Tinti, L. Scognamiglio, M. Michele, E. Casarotti, M. Cattaneo, P. De Gori, C. Chiarabba, G. Monachesi, et al. (2017). The 2016 central Italy seismic sequence: A first look at the mainshocks, aftershocks, and source models, *Seismol. Res. Lett.* **88,** no. 3, 757–771, doi: 10.1785/0220160221.

Cotton, F., R. Archuleta, and M. Causse (2013). What is sigma of the stress drop? *Seismol. Res. Lett.* **84,** no. 1, 42–48.

de Lorenzo, S., A. Zollo, and G. Zito (2010). Source, attenuation, and site parameters of the 1997 Umbria-Marche seismic sequence from the inversion of P wave spectra: A comparison between constant Q(P) and frequency-dependent Q(P) models, *J. Geophys. Res.* **115,** doi: 10.1029/2009JB007004.

Di Bona, M. (2016). A local magnitude scale for crustal earthquakes in Italy, *Bull. Seismol. Soc. Am.* **106,** no. 1, 242–258, doi: 10.1785/0120150155.

Di Stefano, R., E. Kissling, C. Chiarabba, A. Amato, and D. Giardini (2009). Shallow subduction beneath Italy: Three-dimensional images of the Adriatic-European-Tyrrhenian lithosphere system based on high-quality P wave arrival times, *J. Geophys. Res.* **114,** no. B5, doi: 10.1029/2008JB005641.

Eberhart-Phillips, D., and M. Chadwick (2002). Three-dimensional attenuation model of the shallow Hikurangi subduction zone in

the Raukumara Peninsula, New Zealand, *J. Geophys. Res.* **107,** no. B2, 1–15.

Edwards, B., and A. Rietbrock (2009). A comparative study on attenuation and source-scaling relations in the Kanto, Tokai, and Chubu regions of Japan, using data from Hi-net and KiK-net, *Bull. Seismol. Soc. Am.* **99,** doi: 10.1785/0120080292.

Edwards, B., A. Rietbrock, J. J. Bommer, and B. Baptie (2008). The acquisition of source, path, and site effects from microearthquake recordings using Q tomography: Application to the United Kingdom, *Bull. Seismol. Soc. Am.* **98,** 1915–1935.

Efron, B. (1979). Bootstrap methods: Another look at the jackknife, *Ann. Statist.* **7,** no. 1, 1–26, doi: 10.1214/aos/1176344552.

Eshelby, J. D. (1957). The determination of the elastic field of an ellipsoidal inclusion and related problems, *Proc. R. Soc. Lond. Ser. A* **241,** 376–396.

Fletcher, J., J. Boatwright, L. Haar, T. Hanks, and A. McGarr (1984). Source parameters for aftershocks of the Oroville, California, earthquake, *Bull. Seismol. Soc. Am.* **74,** 1101–1123.

Goldstein, P., and A. Snoke (2005). SAC availability for the IRIS community, Incorporated Institutions for Seismology Data Management Center Electronic Newsletter, available at https://ds.iris.edu/ds/newsletter/vol7/no1/193/sac-availability-for-the-iris-community/ (last accessed January 2023).

Golub, G. H., and C. F. Van Loan (1980). An analysis of the total least squares problem, *SIAM J. Numer. Anal.* **17,** 883–893.

Govoni, A., A. Marchetti, P. De Gori, M. Di Bona, F. P. Lucente, L. Improta, C. Chiarabba, A. Nardi, L. Margheriti, N. P. Agostinetti, *et al.* (2014). The 2012 Emilia seismic sequence (northern Italy): Imaging the thrust fault system by accurate aftershock location, *Tectonophysics* **622,** 44–55, doi: 10.1016/j.tecto.2014.02.013.

Hanks, T. C., and H. Kanamori (1979). A moment magnitude scale, *J. Geophys. Res.* **84,** no. B5, 2348–2350.

Helffrich, G., J. Wookey, and I. Bastow (2013). *The Seismic Analysis Code: A Primer and User's Guide*, Cambridge University Press, New York, New York.

Hough, S. E. (1997). Empirical Green's function analysis: Taking the next step, *J. Geophys. Res.* **102,** 5369–5384.

Hough, S. E. (2001). Empirical Green's function analysis of recent moderate events in California, *Bull. Seismol. Soc. Am.* **91,** 456–467.

Ide, S., G. Beroza, S. Prejean, and W. Ellsworth (2003). Apparent break in earthquake scaling because of path and site effects on deep borehole recordings, *J. Geophys. Res.* **108,** 2271, doi: 10.1029/2001JB001617.

Imanishi, K., and W. L. Ellsworth (2006). Source scaling relationships of microearthquakes at Parkfield, CA, determined using the SAFOD pilot hole seismic array, in *Earthquakes: Radiated Energy and the Physics of Faulting*, R. E. Abercrombie, A. McGarr, H. Kanamori, and G. Di Toro (Editors), Vol. 170, American Geophysical Monograph, American Geophysical Union, Washington DC, 81–90, doi: 10.1029/170GM10.

ISIDe Working Group (2007). Italian seismological instrumental and parametric database (ISIDe), Istituto Nazionale di Geofisica e Vulcanologia (INGV), doi: 10.13127/ISIDE.

Kanamori, H., and D. Anderson (1975). Theoretical basis of some empirical relations in seismology, *Bull. Seismol. Soc. Am.* **65,** 1073–1096.

Kane, D. L., G. A. Prieto, F. L. Vernon, and P. M. Shearer (2011). Quantifying seismic source parameter uncertainties, *Bull. Seismol. Soc. Am.* **101,** 535–543, doi: 10.1785/0120100166.

Klinger, A. G., and M. J. Werner (2022). Stress drops of hydraulic fracturing induced microseismicity in the Horn River basin: Challenges at high frequencies recorded by borehole geophones, *Geophys. J. Int.* **228,** no. 3, 2018–2037, doi: 10.1093/gji/ggab458.

Ko, Y., B. Kuo, and S. Hung (2012). Robust determination of earthquake source parameters and mantle attenuation, *J. Geophys. Res.* **117,** no. B4, doi: 10.1029/2011jb008759.

Koulakov, I., D. Bindi, S. Parolai, H. Grosser, and C. Milkereit (2010). Distribution of seismic velocities and attenuation in the crust beneath the North Anatolian fault (Turkey) from local earthquake tomography, *Bull. Seismol. Soc. Am.* **100,** no. 1, 207–224, doi: 10.1785/0120090105.

Lees, J. M., and G. T. Lindley (1994). Three-dimensional attenuation tomography at Loma Prieta: Inversion of t* for Q, *J. Geophys. Res.* **99,** 6843–6863.

Madariaga, R. (1976). Dynamics of an expanding circular fault, *Bull. Seismol. Soc. Am.* **66,** 639–666.

Malagnini, L., L. Scognamiglio, A. Mercuri, A. Akinci, and K. Mayeda (2008). Strong evidence for non-similar earthquake source scaling in central Italy, *Geophys. Res. Lett.* **35,** L17303, doi: 10.1029/2008GL034310.

Mayeda, K., L. Malagnini, and W. R. Walter (2007). A new spectral ratio method using narrow band coda envelopes: Evidence for non-selfsimilarity in the Hector Mine sequence, *Geophys. Res. Lett.* **34,** L11303, doi: 10.1029/2007GL030041.

Mayeda, K., and W. R. Walter (1996). Moment, energy, stress drop, and source spectra of western United States earthquakes from regional coda envelopes, *J. Geophys. Res.* **101,** 11,195–11,208.

Menke, W. (2018). *Geophysical Data Analysis: Discrete Inverse Theory*, Academic Press, San Diego, California.

Michelini, A., and T. V. McEvilly (1991). Seismological studies at Parkfield, part I: Simultaneous inversion for velocity structure and hypocenters using cubic B-splines parameterization, *Bull. Seismol. Soc. Am.* **81,** 524–552.

Oth, A., D. Bindi, S. Parolai, and D. D. Giacomo (2011). Spectral analysis of K-NET and KiK-net data in Japan, part II: On attenuation characteristics, source spectra, and site response of borehole and surface stations, *Bull. Seismol. Soc. Am.* **101,** 667–687.

Oth, A., D. Bindi, S. Parolai, and F. Wenzel (2008). S-wave attenuation characteristics beneath the Vrancea region in Romania: New insights from the inversion of ground-motion spectra, *Bull. Seismol. Soc. Am.* **98,** 2482–2497.

Pacor, F., D. Spallarossa, A. Oth, L. Luzi, R. Puglia, L. Cantore, A. Mercuri, M. D'Amico, and D. Bindi (2016). Spectral models for ground motion prediction in the L'Aquila region (central Italy): Evidence for stress-drop dependence on magnitude and depth, *Geophys. J. Int.* **204,** 697–718, doi: 10.1093/gji/ggv448.

Parolai, S., and A. Oth (2022). On the limitations of spectral source parameter estimation for minor and microearthquakes, *Bull. Seismol. Soc. Am.* **112,** 2364–2375, doi: 10.1785/0120220050.

Pezzo, G., P. De Gori, F. P. Lucente, and C. Chiarabba (2018). Pore pressure pulse drove the 2012 Emilia (Italy) series of earthquakes, *Geophys. Res. Lett.* **45,** 682–690, doi: 10.1002/2017GL076110.

Picozzi, M., A. Oth, S. Parolai, D. Bindi, G. D. Landro, and O. Amoroso (2017). Accurate estimation of seismic source parameters of induced seismicity by a combined approach of generalized inversion and genetic algorithm: Application to the Geysers

geothermal area, California, *J. Geophys. Res.* **122,** no. 5, 3916–3933, doi: 10.1002/2016jb013690.

Prieto, G. A., P. M. Shearer, F. L. Vernon, and D. Kilb (2004). Earthquake source scaling and self-similarity estimation from stacking P and S spectra, *J. Geophys. Res.* **109,** no. B8, doi: 10.1029/2004JB003084.

Rietbrock, A. (2001). P wave attenuation structure in the fault area of the 1995 Kobe earthquake, *J. Geophys. Res.* **106,** 4141–4154.

Scafidi, D., S. Solarino, and C. Eva (2009). P wave seismic velocity and VP=VS ratio beneath the Italian peninsula from local earthquake tomography, *Tectonophysics* **465,** 1–23.

Scherbaum, F. (1990). Combined inversion for the three-dimensional Q structure and source parameters using microearthquake spectra, *J. Geophys. Res.* **95,** 12,423–12,438.

Scognamiglio, L., L. Margheriti, F. M. Mele, E. Tinti, A. Bono, P. De Gori, V. Lauciani, F. P. Lucente, A. G. Mandiello, C. Marcocci, *et al.* (2012). The 2012 Pianura Padana Emiliana seismic sequence: Locations, moment tensors and magnitudes, *Ann. Geophys.* **55,** 549–559.

Shearer, P. M., G. A. Prieto, and E. Hauksson (2006). Comprehensive analysis of earthquake source spectra in southern California, *J. Geophys. Res.* **111,** no. B6, doi: 10.1029/2005JB003979.

Stachnik, J. C., G. A. Abers, and D. H. Christensen (2004). Seismic attenuation and mantle wedge temperatures in the Alaska subduction zone, *J. Geophys. Res.* **109,** doi: 10.1029/2004JB003018.

Stein, S., and M. Wysession (2009). *An Introduction to Seismology, Earthquakes, and Earth Structure*, John Wiley & Sons, Hoboken, New Jersey.

Strollo, A., D. Cambaz, J. Clinton, P. Danecek, C. P. Evangelidis, A. Marmureanu, L. Ottemöller, H. Pedersen, R. Sleeman, K. Stammler, *et al.* (2021). EIDA: The European integrated data archive and service infrastructure within ORFEUS, *Seismol. Res. Lett.* **92,** no. 3, 1788–1795, doi: 10.1785/0220200413.

Toomey, D. R., and G. R. Foulger (1989). Tomographic inversion of local earthquake data from the Hengill-Grensdalur central volcano complex, Iceland, *J. Geophys. Res.* **94,** 17,497–17,510.

Trugman, D. T., and P. M. Shearer (2017). Application of an improved spectral decomposition method to examine earthquake source scaling in southern California, *J. Geophys. Res.* **122,** no. 4, 2890–2910, doi: 10.1002/2017JB013971.

Tsumura, N., A. Hasegawa, and S. Horiuchi (1996). Simultaneous estimation of attenuation structure, source parameter, and site response spectra—Application to the northeastern part of Honshu, Japan, *Phys. Earth Planet. In.* **93,** 105–121.

Tsumura, N., S. Matsumoto, S. Horiuchi, and A. Hasegawa (2000). Three-dimensional attenuation structure beneath the northeastern Japan arc estimated from spectra of small earthquakes, *Tectonophysics* **319,** 241–260.

Valoroso, L., L. Chiaraluce, D. Piccinini, R. Di Stefano, D. Schaff, and F. Waldhauser (2012). Radiography of a normal fault system by 64,000 high-precision earthquake locations: The 2009 L'Aquila (central Italy) case study, *J. Geophys. Res.* **118,** 1–21.

Wang, H., Y. Ren, R. Wen, and P. Xu (2019). Breakdown of earthquake self-similar scaling and source rupture directivity in the 2016–2017 central Italy seismic sequence, *J. Geophys. Res.* **124,** 3898–3917, doi: 10.1029/2018JB016543.

Wessel, P., W. H. Smith, R. Scharroo, J. Luis, and F. Wobbe (2013). Generic mapping tools: Improved version released, *Eos Trans. AGU* **94,** no. 45, 409–410.

Wiemer, S., and M. Wyss (2000). Minimum magnitude of complete reporting in earthquake catalogs: Examples from Alaska, the western United States, and Japan, *Bull. Seismol. Soc. Am.* **90,** 859–869, doi: 10.1785/0119990114.

Yoshimitsu, N., W. L. Ellsworth, and G. C. Beroza (2019). Robust stress drop estimates of potentially induced earthquakes in Oklahoma: Evaluation of empirical Green's function, *J. Geophys. Res.* **124,** 5854–5866, doi: 10.1029/2019JB017483.

Zollo, A., A. Orefice, and V. Convertito (2014). Source parameter scaling and radiation efficiency of microearthquakes along the Irpinia fault zone in southern Apennines, Italy, *J. Geophys. Res.* **119,** 3256–3275, doi: 10.1002/2013JB010116.